BULETINUL INSTITUTULUI POLITEHNIC DIN IAŞI

Volumul 63 (67)
Numărul 2

Secția
MATEMATICĂ
MECANICĂ TEORETICĂ
FIZICĂ

2017 **Editura POLITEHNIUM**

BULETINUL INSTITUTULUI POLITEHNIC DIN IAŞI
PUBLISHED BY
"GHEORGHE ASACHI" TECHNICAL UNIVERSITY OF IAŞI
Editorial Office: Bd. D. Mangeron 63, 700050, Iaşi, ROMANIA
Tel. 40-232-278683; Fax: 40-232-237666; e-mail: polytech@mail.tuiasi.ro

BULETINUL INSTITUTULUI POLITEHNIC DIN IAŞI
BULLETIN OF THE POLYTECHNIC INSTITUTE OF IAŞI
Volumul 63 (67), Numărul 2 2017

Secția

MATEMATICĂ. MECANICĂ TEORETICĂ. FIZICĂ

SUMAR

BULETINUL INSTITUTULUI POLITEHNIC DIN IAŞI
BULLETIN OF THE POLYTECHNIC INSTITUTE OF IAŞI
Volume 63 (67), Number 2 2017

Section

MATHEMATICS. THEORETICAL MECHANICS. PHYSICS

CONTENTS

BULETINUL INSTITUTULUI POLITEHNIC DIN IAŞI
Publicat de
Universitatea Tehnică „Gheorghe Asachi” din Iaşi
Volumul 63 (67), Numărul 2, 2017
Secţia
MATEMATICĂ. MECANICĂ TEORETICĂ. FIZICĂ

SELF-MODULATION OF A HOLLOW CATHODE DISCHARGE PLASMA DYNAMICS I. EXPERIMENTAL

BY

BEDROS ANDREI AGOP[1,*], ŞTEFAN ANDREI IRIMICIUC[2] and DAN GHEORGHE DIMITRIU[2]

[1]“Gheorghe Asachi” Technical University of Iaşi,
Faculty of Material Science and Engineering
[2]“Alexandru Ioan Cuza” University of Iaşi,
Faculty of Physics

Received: June 10, 2017
Accepted for publication: September 25, 2017

Abstract. A discharge plasma with the hollow cathode in form of a spherical grid with a hole was experimentally investigated. Two complex space charge structures appear: a plasma bubble inside the cathode and a fireball localized outside the cathode, near the hole, respectively. These two structures exist in dynamic states, oscillations of the discharge current being recorded. A self-modulation of the plasma system dynamics was evidenced in the time series of discharge current oscillations. This phenomenon is due to the dependence of the oscillations frequency on the current and the coupling between the two structures through the plasma.

Keywords: plasma; hollow cathode; self-modulation; fireball.

[*]Corresponding author; *e-mail*: andrei.agop@yahoo.com

1. Introduction

According to National Aeronautics and Space Administration (NASA), European Space agency (ESA), Japan Aerospace Exploration Agency (JAXA), Marshall Space Flight Centre, etc., one of the main objectives of the future aerospace missions will be focused on the next generation of microsatellites (Alderson *et al*., 2003). Also, NASA and ESA space technology programs, like Gravity Recovery and Climate Experiment (GRACE), Gravity Field and Steady-State Ocean Circulation Explorer (GOCE), Microscope, or Laser Interferometer Space Antenna (LISA) Pathfinder, emphasized the importance of small spacecraft as dominant trend in aerospace. Both the microsatellites and the small spacecraft will need novel propulsion technologies.

Plasma thrusters proved to be good candidates for space propulsion, since they deliver a high specific impulse and allow long-term space missions (Lemmer, 2017). Ion and Hall thrusters use hollow cathodes and the properties of the cathode material, the geometry of the hollow cathode and the structure of the cathode plasma determine the performance and life of both types of thrusters (Goebel and Katz, 2008).

Here we report on the experimental investigation of a hollow cathode discharge plasma that can be suitable for application as plasma thruster. The cathode is a spherical grid with a hole. The Paschen's curve and the current-voltage characteristics of the discharge were obtained in order to establish the working parameters of the discharge. During the discharge, two complex space charge structures appear: a plasma bubble inside the cathode and a fireball outside the cathode, near the hole. These structures exist in dynamic states, oscillations of the discharge current being recorded. A self-modulation of the plasma system dynamics was evidenced in the time series of the discharge current, due to the coupling between the individual dynamics of the two complex space charge structures.

2. Experimental Results and Discussion

The experiments were performed into the hollow cathode discharge plasma diode from Self-Organization Laboratory of the Faculty of Physics, "Alexandru Ioan Cuza" Univeristy of Iași, Romania, schematically shown in Fig. 1. The diode is made by glass, the anode is a rectangular tantalum plate of 25 cm × 20 cm size, while the cathode is a spherical metallic grid with a diameter of 4 cm (with 0.5 mm the diameter of the metallic wires and 2 mm the mesh width), having a small hole with the diameter of about 6 mm on one side. The distance between the cathode and anode is d = 25 cm. For experiments, argon has been used as working gas.

To establish the optimal parameters for the discharge, the Paschen's curve was obtained by recording the discharge breakdown voltage function of

the gas pressure, the distance between the anode and the cathode being kept constant. The result is shown in Fig. 2, from which it can be observed that the minimum of the breakdown voltage, of approximate 300 V, corresponds to a value of the argon pressure of approximate 10^{-1} mbar.

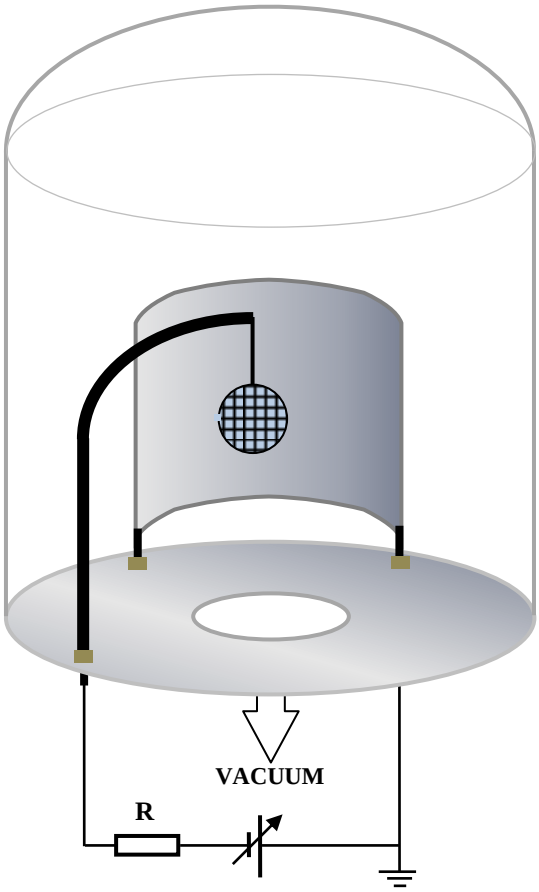

Fig. 1 – Experimental setup.

Fig. 3 shows the static current-voltage (*I-V*) characteristic of the discharge, obtained by recording the dc component of the discharge current simultaneously with the increasing and subsequent decreasing of the voltage applied to the discharge. By changing the discharge voltage, the complex space charge structures inside and around the hollow cathode pass through different stages. Thus, at the increasing of the discharge voltage, after the small current jump A→B (see *I-V* characteristic in Fig. 3), a diffuse spherical structure appears inside the cathode, while a strong electron beam escape from inside the cathode through the hole, producing excitations and ionizations of the gas atoms

along the direction of propagation (see photo in Fig. 4*a*). In this stage, there is no breakdown of the discharge, but the increasing of the current is due only to the ionizations of the gas atoms inside the cathode, amplified by the hollow cathode effect, and to the electrons escaping from the cathode through the hole, which produce local ionizations of the gas atoms along the direction of propagation. The plasma bubble (Stenzel and Urrutia, 2012a, b, c, d) inside the cathode appears due to the electron-neutral impact excitations and ionizations processes, a high density of electrons existing there because of the hollow cathode effect.

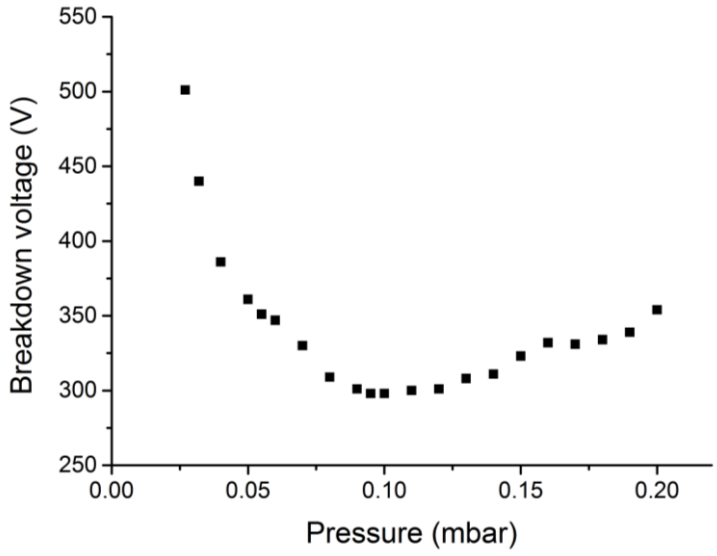

Fig. 2 – Paschen's curve for argon and 25 cm distance between the cathode and anode.

By further increasing the discharge voltage, a strong jump of the current appears in the current-voltage characteristic (marked by C→D in Fig. 3), corresponding to the breakdown of the discharge. In Fig. 4*b* it can be observed the negative glow of the discharge around the cathode, which is coupled with the bubble inside the cathode through an asymmetric fireball. The right part (towards the cathode) of this fireball is smaller and penetrates inside the cathode through the hole, while its left part (towards the negative glow of the discharge) is larger and diffuse into the negative glow. The increase of the voltage up to the discharge breakdown voltage leads to an increase of the luminous intensity of the structures (see Fig. 4*c*), while the fireball becomes more and more asymmetric, its left part strongly increasing and expanding into the negative glow of the discharge, while the right part is expulsed outside the cathode in the vicinity of the hole.

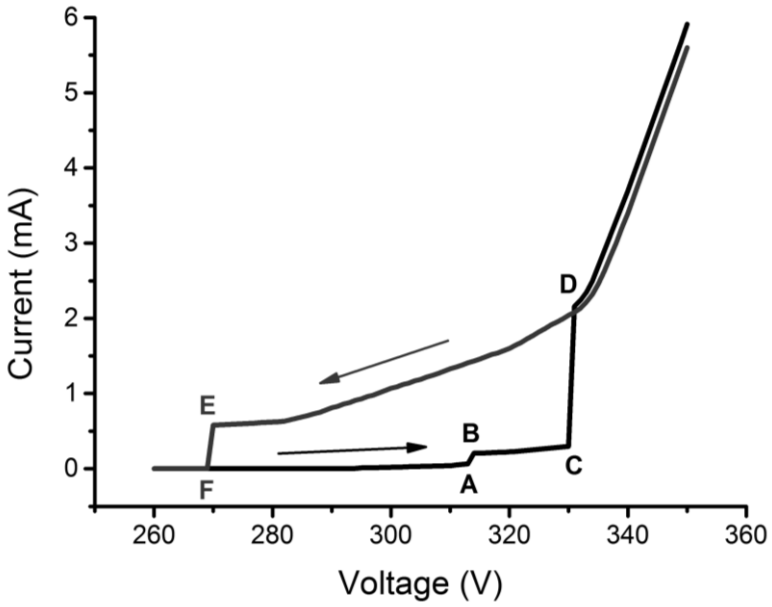

Fig. 3 – Static current-voltage characteristic of the discharge.

a

b

c

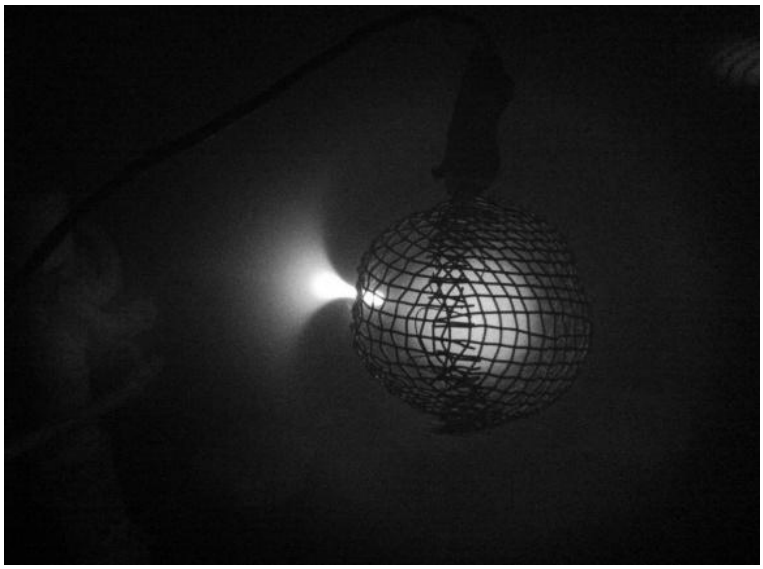

d

Fig. 4 – Photos of the complex space charge structures inside and around the cathode, in different stages of their development.

When the discharge voltage is decreased, a large hysteresis (of about 60 V) can be observed (as expected) in the static *I-V* characteristic of the discharge (Fig. 3), in connection with the breakdown and quenching of the discharge. The fireball decreases in dimension and luminosity, being almost symmetrical (see photo of the structure in Fig. 4*d*). Its right part penetrates again inside the cathode. In this state, on the branch D→E of the static *I-V* characteristic (Fig. 3), interesting nonlinear dynamic phenomena were observed by investigating the time series of the discharge current oscillations.

The time series of the discharge current oscillations were recorded with a sampling rate of 2.5 GS/s. Fig. 5 shows such a time series, recorded for a discharge voltage value U = 289 V. Fig. 6 shows details from this time series (on the left column) and their corresponding fast Fourier transforms (FFT) (on the right column). Different dynamic states can be observed. These states are the result of the nonlinear interaction between the individual dynamics of inner plasma bubble and the fireball, respectively. Both structures exist in dynamic states, the oscillation frequency depending on the value of the current (Stenzel and Urrutia, 2012a, b, c, d; Niculescu *et al.*, 2010). The inner plasma bubble periodically release bunches of electrons, which act as forcing drive of the oscillating fireball. The fireball passes through different dynamic states as the

forcing frequency changes because of the modification of the discharge current value. In other words, the forcing frequency determines the dynamic state, *i.e*. the amplitude and frequency of the discharge current oscillations, which, at their turn, modify the frequency of the inner bubble dynamics, *i.e.* the forcing frequency. In this way, a continuous self-modulation of the plasma system dynamics exists, as can be observed in Figs. 5 and 6.

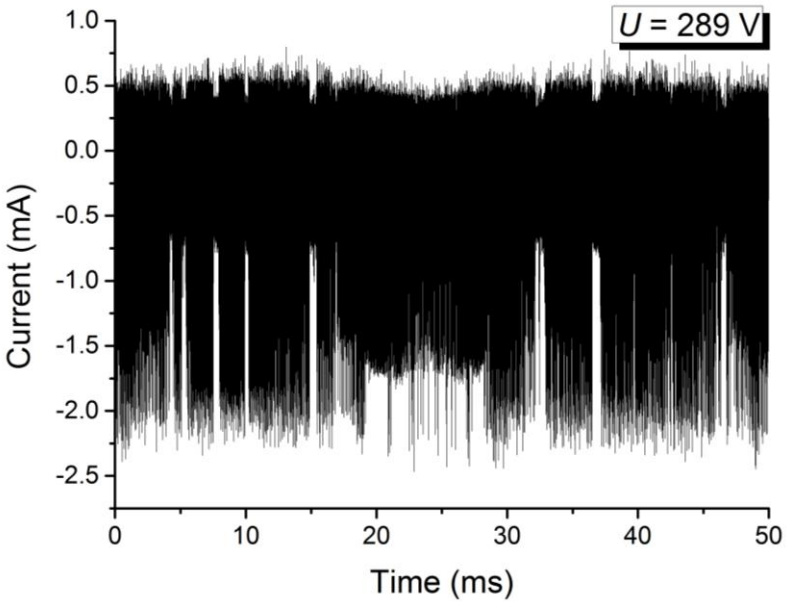

Fig. 5 – Time series of the discharge current oscillations for the value of the discharge voltage U = 289 V.

3. Conclusions

A hollow cathode discharge plasma was experimentally investigated, the cathode being a spherical metallic grid with a hole. Two complex space charge configuration appears, namely a plasma bubble inside the cathode and a fireball outside the cathode, near the hole. The static current-discharge characteristics evidenced two current jumps and a strong hysteresis, related to different states of the discharge plasma. Self-modulation of the plasma system dynamics was evidenced in the time series of the discharge current oscillations, due to the nonlinear interaction of the individual dynamics of the complex space charge structures.

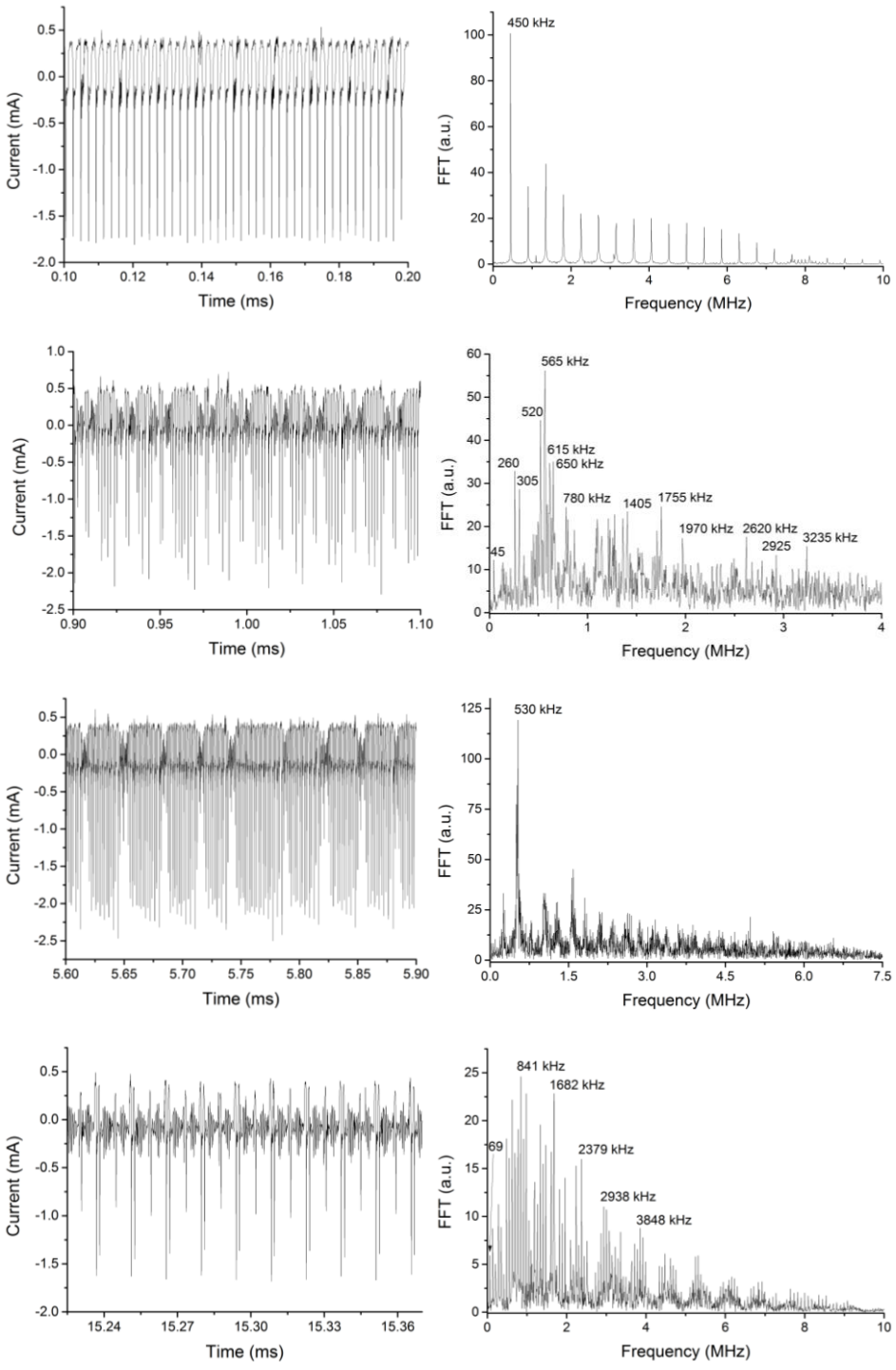
Current (mA)
Time (ms)
FFT (a.u.)
Frequency (MHz)
450 kHz
565 kHz
520
615 kHz
650 kHz
260
305
780 kHz
1405
1755 kHz
1970 kHz
2620 kHz
2925
3235 kHz
45
530 kHz
841 kHz
1682 kHz
69
2379 kHz
2938 kHz
3848 kHz

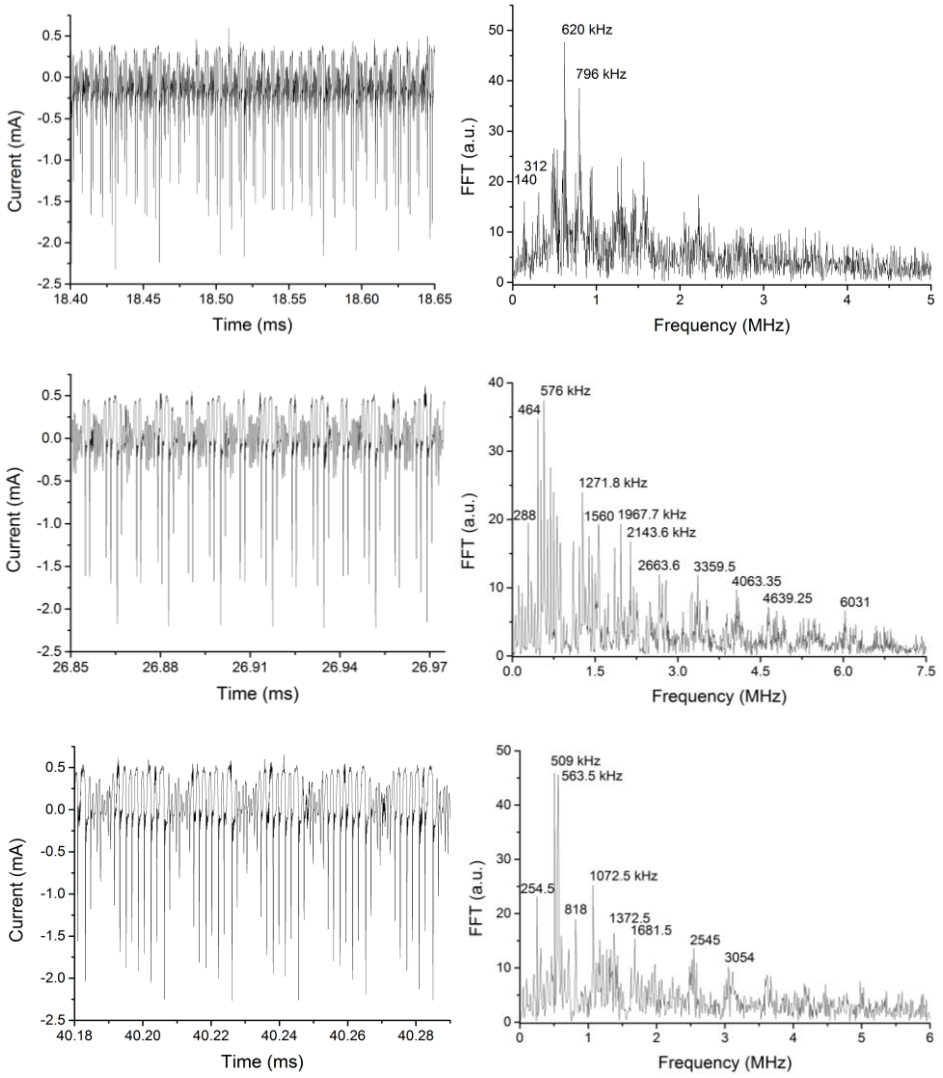

Fig. 6 – Details of the time series of the discharge current oscillations from Fig. 5 (left column) and their corresponding FFTs (right column).

REFERENCES

Alderson L., Chaloner C., Howieson J., *ESA's Advanced Microsatellite Mission (AMM) Study*, Acta Astronaut, **52**, 897-903 (2003).

Goebel D.M, Katz I., *Fundamentals of Electric Propulsion: Ion and Hall Thrusters*, John Wiley & Sons, Hoboken, New Jersey, 2008.

Lemmer K., *Propulsion for CubeSats*, Acta Astronaut., **134**, 231-243 (2017).

Niculescu O., Dimitriu D.G., Paun V.P., Matasaru P.D., Scurtu D., Agop M., *Experimental and Theoretical Investigations of a Plasma Fireball Dynamics*, Phys. Plasmas, **17**, 042305 (2010).

Stenzel R.L., Urrutia J.M., *Oscillating Plasma Bubble. I. Basic Properties and Instabilities*, Phys. Plasmas, **19**, 082105 (2012a).

Stenzel R.L., Urrutia J.M., *Oscillating Plasma Bubble. II. Pulsed Experiments*, Phys. Plasmas, **19**, 082106 (2012b).

Stenzel R.L., Urrutia J.M., *Oscillating Plasma Bubble. III. Internal Electron Sources and Sinks*, Phys. Plasmas, **19**, 082107 (2012c).

Stenzel R.L., Urrutia J.M., *Oscillating Plasma Bubble. IV. Grids, Geometry, and Gradients*, Phys. Plasmas, **19**, 082108 (2012d).

AUTOMODULAREA DINAMICII UNEI PLASME DE DESCĂRCARE CU CATOD CAVITAR
I. Experiment

(Rezumat)

A fost investigată experimental o plasmă de descărcare cu catod cavitar sub forma unei grile sferice cu un orificiu. S-a observat apariția a două structuri complexe de sarcini spațiale: o bulă de plasmă în interiorul catodului, respectiv o minge de foc localizată în exteriorul catodului, în vecinătatea orificiului. Aceste două structuri se află în stare dinamică, fiind înregistrate oscilații ale curentului de descărcare. În seriile temporale corespunzătoare oscilațiilor curentului de descărcare a fost evidențiat un fenomen de automodulare a dinamicii sistemului cu plasmă. Acest fenomen se datorează dependenței frecvenței oscilațiilor de valoarea curentului, precum și cuplajului prin plasmă a celor două structuri.

BULETINUL INSTITUTULUI POLITEHNIC DIN IAŞI
Publicat de
Universitatea Tehnică „Gheorghe Asachi” din Iaşi
Volumul 63 (67), Numărul 2, 2017
Secţia
MATEMATICĂ. MECANICĂ TEORETICĂ. FIZICĂ

SELF-MODULATION OF A HOLLOW CATHODE DISCHARGE PLASMA DYNAMICS II. THEORETICAL MODELING

BY

ŞTEFAN ANDREI IRIMICIUC[1], DAN GHEORGHE DIMITRIU[1] and BEDROS ANDREI AGOP[2,*]

[1]“Alexandru Ioan Cuza” University of Iași,
Faculty of Physics
[2]“Gheorghe Asachi” Technical University of Iași,
Faculty of Material Science and Engineering

Received: June 15, 2017
Accepted for publication: September 25, 2017

Abstract. A theoretical model is proposed, in the frame of Scale Relativity Theory, able to explain the phenomenon of self-modulation of a hollow cathode discharge plasma dynamics. In this model, the complexity of the interactions in the plasma volume was replaced by non-differentiability (fractality). Discharge plasma particles move free, without any constrains, on continuous but non-differentiable curves in a fractal space. A Riccati type differential equation was obtained, describing the dynamics of a harmonic oscillator. The solution of this equation shows a frequency modulation through a Stoler transformation. The obtained results are in good agreement with the experimental ones.

Keywords: non-differentiability; Scale Relativity Theory; fractal; self-modulation.

[*]Corresponding author; *e-mail*: andrei.agop@yahoo.com

1. Introduction

Plasma discharges can be assimilated to complex systems taking into account their structural-functional duality (Mitchell, 2009). The standard models (fluid model, kinetic model, etc.) (Morozov, 2012; Chen, 2016) used to study the plasma discharges dynamics are based on the hypothesis of differentiability of the physical variables that describe it, such as energy, momentum, density, etc. But differential methods fail when facing the physical reality, such as instabilities of the discharge plasma that can generate chaos or patterns through self-structuring, by means of the non-differentiable (fractal) method (Mandelbrot, 1982; Hastings and Sugihara, 1993; Falconer, 2014).

In order to describe some of the dynamics of plasma discharges by means of non-differentiable method, and still remain treatable as differential method, it is necessary to introduce the scale resolution, both in the expressions of the physical variables and the dynamics equations. This means that any dynamic variable become dependent also on the scale resolution. Such a physical theory was developed both in the Scale Relativity Theory with fractal dimension equals with 2 (Nottale, 1993; Nottale, 2011) and with an arbitrary constant fractal dimension (Dimitriu *et al.*, 2015; Merches and Agop, 2016). In the field of plasma discharges, if we assume that the complexity of interactions in the plasma volume is replaced by non-differentiability (fractality), the constrained motions on continuous and differentiable curves in a Euclidian space of the plasma discharge particles are replaced with the free motions, without any constrains, on continuous but non-differentiable curves in a fractal space of the same discharge plasma particles. This is the reasoning by which, at time resolution scales large by comparing with the inverse of the highest Lyapunov exponent, the deterministic trajectories are replaced by a collection of potential states, so that the concept of "definite position" is substituted by that of an ensemble of positions having a definite probability density. As a consequence, the determinism and the potentiality (non-determinism) become distinct parts of the same "evolution" of discharge plasma, through reciprocal interactions and conditioning, in such a way that the plasma discharge particles are substituted with the geodesics themselves (Arnold, 1989; Hillborn, 2000).

In the present paper, a non-differentiable theoretical model is developed, able to explain the phenomenon of self-modulation of a plasma dynamics, experimentally observed in a hollow cathode discharge in connection with the development of two space charge structures.

2. Theoretical Model and Discussion

In the frame of Scale Relativity Theory with an arbitrary constant fractal dimension, the dynamics of discharge plasma can be described by means of the covariant derivatives (Nottale, 2011):

$$\frac{\hat{d}}{dt}=\partial_t+\hat{V}^l\partial_l+\frac{1}{4}(dt)^{\frac{2}{D_F}-1}D^{lk}\partial_l\partial_k, \tag{1}$$

where

$$\begin{aligned}&\partial_t=\frac{\partial}{\partial t},\quad \partial_l=\frac{\partial}{\partial X^l},\quad \partial_l\partial_k=\frac{\partial^2}{\partial X^l\partial X^k}\\&D^{lk}=\left(\lambda_+^l\lambda_+^k\pm\lambda_-^l\lambda_-^k\right)-i\left(\lambda_+^l\lambda_+^k\pm\lambda_-^l\lambda_-^k\right).\\&\hat{V}^l=V^l-iU^l,\quad i=\sqrt{-1}\end{aligned} \tag{2}$$

In the above relations X^l are the spatial fractal coordinates, t is the non-fractal time coordinate, having the role of motion curve affine parameter, dt is the resolution scale, $\hat{V}^l$ is the velocity complex field, V^l is the differentiable component of the velocity complex field, which is independent on the resolution scale, U^l is the non-differentiable component of the velocity complex field, which is dependent on the resolution scale, D^{lk} is the fractal – non-fractal transition pseudo-tensor, dependent, through stochastic fractalization, either on the "forward physical processes" λ_+^l, or the "backward physical processes" λ_-^l, D_F is the fractal dimension of the motion curves. For D_F one can choose different definitions, *i.e.* the fractal dimension in a Kolmogorov sense, Hausdorff-Besikovici sense, etc. (Mandelbrot, 1982; Barnsley, 1993), but once chosen a definition, it has to remain constant during the whole analysis of the discharge plasma dynamics.

For fractalization through Markov type stochastic processes, *i.e.* for Levy type movement of the discharge plasma particles (Mandelbrot, 1982; Barnsley, 1993), the fractal – non-fractal transition pseudo-tensor becomes

$$D^{lk}=\pm 4i\lambda\delta^{lk}, \tag{3}$$

where λ is the "diffusion coefficient" associated to the fractal – non-fractal transitions (Merches and Agop, 2016) and δ^{lk} is the Kronecker pseudo-tensor. In this case, the scale covariant derivative (1) takes the form

$$\frac{\hat{d}}{dt}=\partial_t+\hat{V}^l\partial_l\pm i\lambda(dt)^{\frac{2}{D_F}-1}\partial_l\partial^l. \tag{4}$$

Postulating now the scale covariance principle, according to which the physics laws in their simplest representation are remaining invariant with respect to the scale transformations, the states' density conservation law becomes

$$\frac{\hat{d}\rho}{dt} = \partial_t \rho + \hat{V}^l \partial_l \rho \pm i\lambda (dt)^{\frac{2}{D_F}-1} \partial_l \partial^l \rho = 0, \tag{5}$$

or more, separating the movement on the scale resolution

$$\partial_t \rho + V^l \partial_l \rho = 0 \tag{6}$$

for the differentiable scale resolution and

$$-U^l \partial_l \rho \pm \lambda (dt)^{\frac{2}{D_F}-1} \partial_l \partial^l \rho = 0 \tag{7}$$

for the non-differentiable scale resolution. From such a perspective, the fractal – non-fractal dynamic transition of the states' density can be obtained by summing Eqs. (6) and (7), taking the form:

$$\partial_t \rho + \left(V^l - U^l\right) \partial_l \rho \pm \lambda (dt)^{\frac{2}{D_F}-1} \partial_l \partial^l \rho = 0. \tag{8}$$

From here, by means of compactification of the movements at the two scale resolutions $V^l = U^l$, the fractal type diffusion equation become:

$$\partial_t \rho - \lambda (dt)^{\frac{2}{D_F}-1} \partial_l \partial^l \rho = 0. \tag{9}$$

Let us now use Eq. (9) to analyze the dynamic of an electron beam accelerated in a strong electric field which impinges onto a neutral medium. As a result of these interactions, ionizations are produced both by the primary electrons (from the beam), αj, where α is the primary ionization coefficient and j is the beam current density, and by the secondary electrons which result from the direct ionization processes, $\beta j \rho_e$, with β the secondary ionization coefficient and ρ_e the electron density. In these conditions, the focus is placed on the study of the dynamics induced only by the electronic branch, through Eq. (9) written in the following form:

$$\partial_t \rho_e + \lambda (dt)^{\frac{2}{D_F}-1} \partial_l \partial^l \rho_e = -\alpha j - \beta j \rho_e. \tag{10}$$

Since the previous dynamics implied a one-dimensional symmetry, Eq. (10), by means of substitutions

$$\alpha j + \beta j \rho_e = Kq, \quad \tau = \frac{x}{v} - t, \quad M = \frac{K}{\beta j v^2} \lambda (dt)^{\frac{2}{D_F}-1}, \quad 2Rw = -\frac{K}{\beta j}, \tag{11}$$

becomes a damped harmonic oscillator type equation:

$$M\ddot{q} + 2R\dot{q} + Kq = 0\,. \tag{12}$$

Rewritten as

$$\begin{aligned} \dot{p} &= -\frac{2R}{M}p - \frac{K}{M}q\,, \\ \dot{q} &= p \end{aligned} \tag{13}$$

Eq. (12) induces a two-dimensional manifold of phase space type (p,q), in which p would corresponds to a "momentum" type variable and q to a "position" type one. Then, the parameters M, R and K can have the following significance:

i) M represents the "matricidal" type effects through the connection with ionization processes (both global, described by $\alpha j + \beta j$, and local, described by βj) and through the fractal diffusion (described by $\lambda(dt)^{\frac{2}{D_F}-1}$). All these are done with respect to a travelling wave type movement based on the self-similar dynamic solutions ($\tau = \frac{x}{v} - t$);

ii) R represents the "dissipative" type effects through the connection with the ionization processes (both global, described by $\alpha j + \beta j$, and local, described by βj);

iii) K represents the "structural" type effects in connection with the ionization processes (only the global ones, described by $\alpha j + \beta j$).

The second equation from (13) corresponds to the momentum definition. Eqs. (13) do not represents a Hamiltonian system, since the associated matrix is not an involution (the matrix trace is not null). This statement becomes clearer if we put the system in its matrix form:

$$\begin{pmatrix} \dot{p} \\ \dot{q} \end{pmatrix} = \begin{pmatrix} -2\frac{R}{M} & -\frac{K}{M} \\ 1 & 0 \end{pmatrix} \begin{pmatrix} p \\ q \end{pmatrix}. \tag{14}$$

As long as M, R and K have constant values, this matrix equation written in the equivalent form evidences the position of the energy and thus of the Hamiltonian, which is, for this particular case, identified with the energy of the system obviously only for the cases in which the energy can be identified with the Hamiltonian. Indeed, from Eq. (14) it can be obtained

$$\frac{1}{2}M\left(p\dot{q}-q\dot{p}\right)=\frac{1}{2}\left(Mp^2+2Rpq+Kq^2\right), \tag{15}$$

which proves that the energy in its quadratic form (the right hand of Eq. (15)) is the variation rate of the physical action, represented by the elementary area from the phase space. From here it results that the energy does not have to obey the conservation laws in order to act like a variation rate for the physical action.

On can ask now what could be the conservation law, if it exists. To give an adequate answer, we first observe that Eq. (15) can be written as a Riccati type differential equation

$$\dot{w}+w^2+2\mu w+w_0^2=0, \tag{16}$$

with

$$w=\frac{p}{q},\quad \mu=\frac{R}{M},\quad \omega_0^2=\frac{K}{M}. \tag{17}$$

Furthermore let us note that Riccati type Eq. (16) always represents a Hamiltonian system describing harmonic oscillator type dynamic

$$\begin{pmatrix}\dot{p}\\ \dot{q}\end{pmatrix}=\begin{pmatrix}-\frac{R}{M} & -\frac{K}{M}\\ 1 & \frac{R}{M}\end{pmatrix}\begin{pmatrix}p\\ q\end{pmatrix}. \tag{18}$$

This is a general characteristic describing the Riccati type equation and the Hamiltonian's dynamic (Arnold, 1989; Libermann and Marle, 1987). Eq. (9) can be reobtained by bulding from Eq. (18) the 1- differential form for the elementary area from the phase space for harmonic oscillator type dynamic. Regarding Eq. (15), it can be integrated by specifying the fact that the energy does not conserve anymore, but we find that another more complicated dynamics variable will be conserved (Denman, 1968):

$$\frac{1}{2}\left(Mp^2+2Rpq+Kq^2\right)\exp\left[\frac{2R}{\sqrt{MK-R^2}}\arctan\left(\frac{Mp+Rq}{q\sqrt{MK-R^2}}\right)\right]=\text{const}. \tag{19}$$

It results that the energy is conserved in a classical meaning when either R becomes null, or the movement in the phase space is characterized by the line passing through origin and having the slope defined by the ratio between R and

M. Moreover, by comparing with the case of thermal radiation regarding the distribution function on a pre-established "local oscillators" ensemble, it results

$$P(r,w)=\frac{1}{1+2rw+w^2}\exp\left\{\frac{2r}{\left(1-r^2\right)^{1/2}}\arctan\left[\frac{w\left(1-r^2\right)^{1/2}}{1-rw}\right]\right\}, \tag{20}$$

where r is the correlation coefficient and $w^2=\frac{\varepsilon_0}{u}$ is the ratio between the thermal energy quanta, ε_0, and the reference energy, u. Eq. (19) can be rewritten as:

$$\frac{Kq^2}{2}=\frac{\text{const}}{1+2rw+w^2}\exp\left\{\frac{2r}{\left(1-r^2\right)^{1/2}}\arctan\left[\frac{w\left(1-r^2\right)^{1/2}}{1-rw}\right]\right\}, \tag{21}$$

with

$$w^2=\frac{Mp^2}{Kq^2},\quad r^2=\frac{R}{K}. \tag{22}$$

From here we can emphasis the statistic character of the energy: the potential energy is constructed as a functional of a specific statistical variable. This variable is given by the ratio between the kinetic energy and the potential one of the local oscillator.

Thus, we propose here such a "quantization" procedure (see Fig. 1a and 1b) through the correlation of all statistical ensembles associated with "local oscillators" (Ioannidou, 1983), induced by mean of the condition

$$P(r,1)=\frac{e^{-\frac{\varepsilon_0}{kT}}}{2(1+r)}\exp\left[\frac{2r}{\left(1-r^2\right)^{1/2}}\arctan\left(\sqrt{\frac{1+r}{1-r}}\right)\right], \tag{23}$$

where k is the Boltzmann constant and T is the characteristic temperature of the thermal radiation, representing explicitly the connection between the "quanta" and the statistical correlation of the process represented by the thermal radiation. Moreover, the previous relation does not explicitly specifies the expression of the "quanta" in the weak correlation limit since as for $r \to 0$ it implies $\varepsilon_0 \to kT\ln 2$. In such a limit, the quanta and thus the frequency ν (through $\varepsilon_0 = h\nu$, where h is the Planck constant) is proportional with the

"color" temperature. We note that in our case the thermal radiation is identified with the thermodynamic equilibrium plasma radiation.

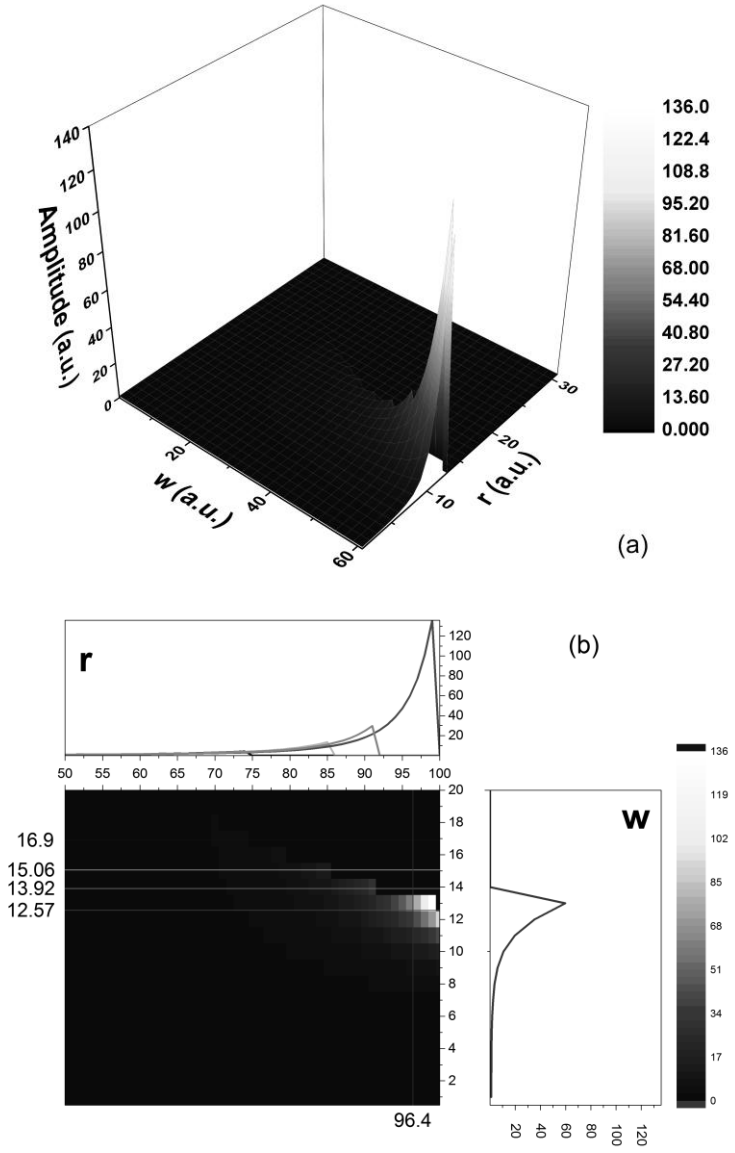

Fig. 1 – "Quantization" procedure through correlation of all statistical ensembles associated with "local oscillators": 3D dependences (*a*) and the contour plot (*b*).

Since we are focused on identifying the dissipative forces, we will present a physical significance for the Riccati Eq. (16) by means of its

associated Hamiltonian system (18). Let us observe that Eq. (12) is the expression of a variation principle

$$\delta\int_{t_0}^{t_1} L dt = 0 \tag{24}$$

regarding the Lagrangian

$$L(q,\dot{q},t) = \frac{1}{2}\left(M\dot{q}^2 - Kq^2\right)\exp\left(\frac{2R}{M}t\right). \tag{25}$$

This represents the Lagrangian form of a harmonic oscillator with explicit time dependent parameters. The Lagrangian integral defined on a finite interval $[t_0,t_1]$ is the physical action of an oscillator during that specific time interval, describing the difference between the kinetic and potential energy, respectively. In order to obtain Eq. (12), it is necessary to consider the variation of this action under the explicit condition in such a way that the variance of the coordinate at the interval extremes is null:

$$\delta q\big|_{t_0} = \delta q\big|_{t_1} = 0. \tag{26}$$

Even so, in order to obtain a closed trajectory, we need to impose a supplementary condition, for instance that the values of the coordinates at the interval extremes are identical:

$$q(t_0) = q(t_1). \tag{27}$$

Moreover, if this trajectory is closed in the phase space, it will result that the same condition will be true also for velocities.

Let us focus now on the movement principle and on the movement equation. The Lagrangian is defined until an additive function, which needs to be derivative in respect to the time of another function. The procedure is largely used in theoretical physics by defining the gauge transformation. Let's define a gauge transformation in which the Lagrangian is a perfect square. This is known and explored in the control theory (Zelkin, 2000). The procedure consists in adding the following term to Lagrangian

$$\frac{1}{2}\frac{d}{dt}\left[wq^2\exp\left(\frac{2R}{M}t\right)\right], \tag{28}$$

where w is a continuous function in time, so that the Lagrangian is a perfect square. The function variation given by the derivative operator is null, only due to

the conditions presented in Eq. (27), thus the motion equation does not change. The new Lagrangian written in relevant coordinates takes the following form:

$$L(\dot{q},q,t)=\frac{M}{2}\left(\dot{q}+\frac{w}{M}q\right)^2\exp\left(\frac{2R}{M}t\right), \tag{29}$$

with the condition that *w* need to satisfy the following Riccati type equation:

$$\dot{w}-\frac{1}{M}w^2+\frac{2R}{M}w-K=0. \tag{30}$$

Lagrangian depicted in Eq. (29) will be considered here as representing the whole energy of the system. As before, there is a relationship between the Riccati Eq. (30) and the Hamiltonian dynamics. Henceforth we will find a relation similar to that one presented in Eq. (18):

$$\begin{pmatrix}\dot{\eta}\\ \dot{\xi}\end{pmatrix}=\begin{pmatrix}-\frac{R}{M} & -\frac{K}{M}\\ 1 & \frac{R}{M}\end{pmatrix}\begin{pmatrix}\eta\\ \xi\end{pmatrix}, \tag{31}$$

with $w=\frac{\eta}{\xi}$. This system is obviously a Hamiltonian one. Thus, we can identify the factors of *w* as the phase space coordinates. Eq. (30) specifies the fact that *w* is a dissipation coefficient, more precisely a mass variation rate for the variable mass case. It is important to find the most general solution of this equation. Cariñena and Ramos (Cariñena and Ramos, 2000) presented a modern approach to integrate a Riccati equation. Let's consider the next complex numbers:

$$w_0\equiv R+iM\Omega,\quad w_0^*\equiv R-iM\Omega,\quad \Omega^2=\frac{K}{M}-\left(\frac{R}{M}\right)^2. \tag{32}$$

The roots of the quadratic polynomial from the left hand side of Eq. (30) are two constant solution of the equation. Being constant, their derivatives are null, thus the polynomial is also null. In order to avoid this, we first perform the homograph transformation:

$$z=\frac{w-w_0}{w-w_0^*}. \tag{33}$$

In these conditions, it results z is a solution of the linear and homogeneous first order equation:

$$\dot{z} = 2i\Omega z \quad \Rightarrow \quad z(t) = z(0)e^{2i\Omega t}. \tag{34}$$

Hence, if we express the initial condition $z(0)$ in a right manner, we can obtain the general solution of Eq. (30) by applying an inverse transformation to Eq. (33). We find

$$w = \frac{w_0 + re^{2i\Omega(t-t_r)}w_0^*}{1 + re^{2i\Omega(t-t_r)}}, \tag{35}$$

where r and t_r are two real constants characterizing the solution. Using relations (32), we can put the same solution in real terms:

$$z = R + M\Omega\left\{\frac{2r\sin\left[2\Omega(t-t_r)\right]}{1+r^2+2r\cos\left[2\Omega(t-t_r)\right]} + i\frac{1-r^2}{1+r^2+2r\cos\left[2\Omega(t-t_r)\right]}\right\}. \tag{36}$$

This relationship shows a frequency modulation through a Stoler transformation (Stoler, 1970) which leads to the complex representation of this parameter.

Fig. 2 shows the dimensionless discharge current oscillations, obtained from the solution (36) for different scale resolutions of the frequency, r being kept constant at the value 0.1. We observe that for small scale resolutions the current is described by a simple oscillatory regime, while as the frequency scale resolution increases we notice the appearance of some patterns. The patterns become denser and foreshadow the presence of modulation of the oscillating frequency.

From Fig. 2 we can extract time series of the discharge current oscillations for different value of ω, which are shown in Fig. 3. We notice that these signals are similar to that experimentally recorded.

Fig. 4 shows the time series of the discharge current oscillations for different values of r and for two values of the oscillations frequency, ω. The damping of the oscillatory state describes the losses through dissipative or dispersive mechanisms. In Fig. 4 competing oscillatory behaviors described by two oscillations frequencies, with comparable amplitudes, can be identified. As the damping increases, the ratio between the two oscillation frequencies changes, the system ending in an oscillatory state on a single frequency. These results are also in good agreement with the experimental ones.

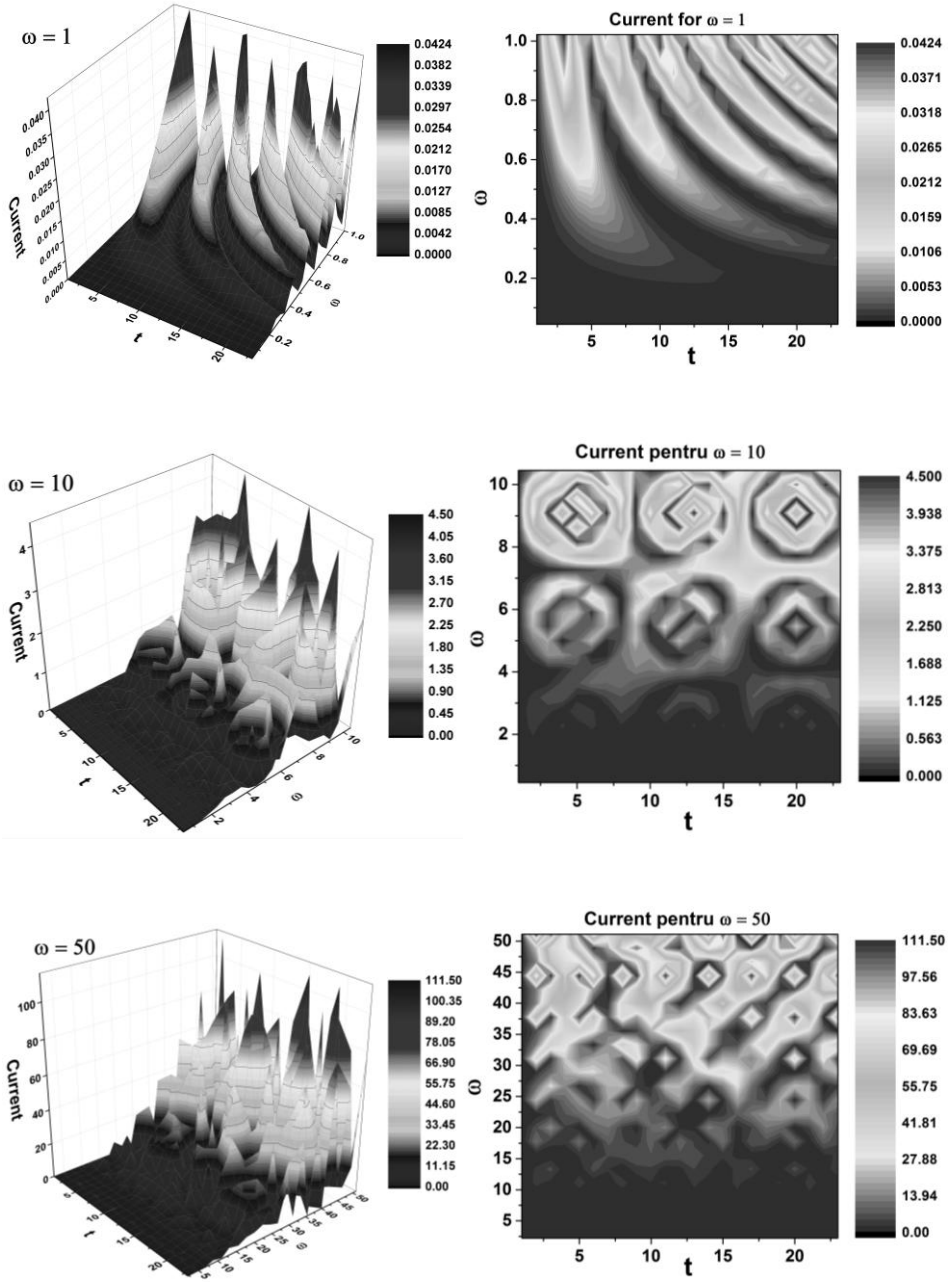

Fig. 2 – Dimensionless discharge current obtained from the theoretical model, for different scale resolutions of the oscillations frequency (3D maps on the left column and the contour plots on the right column, respectively).

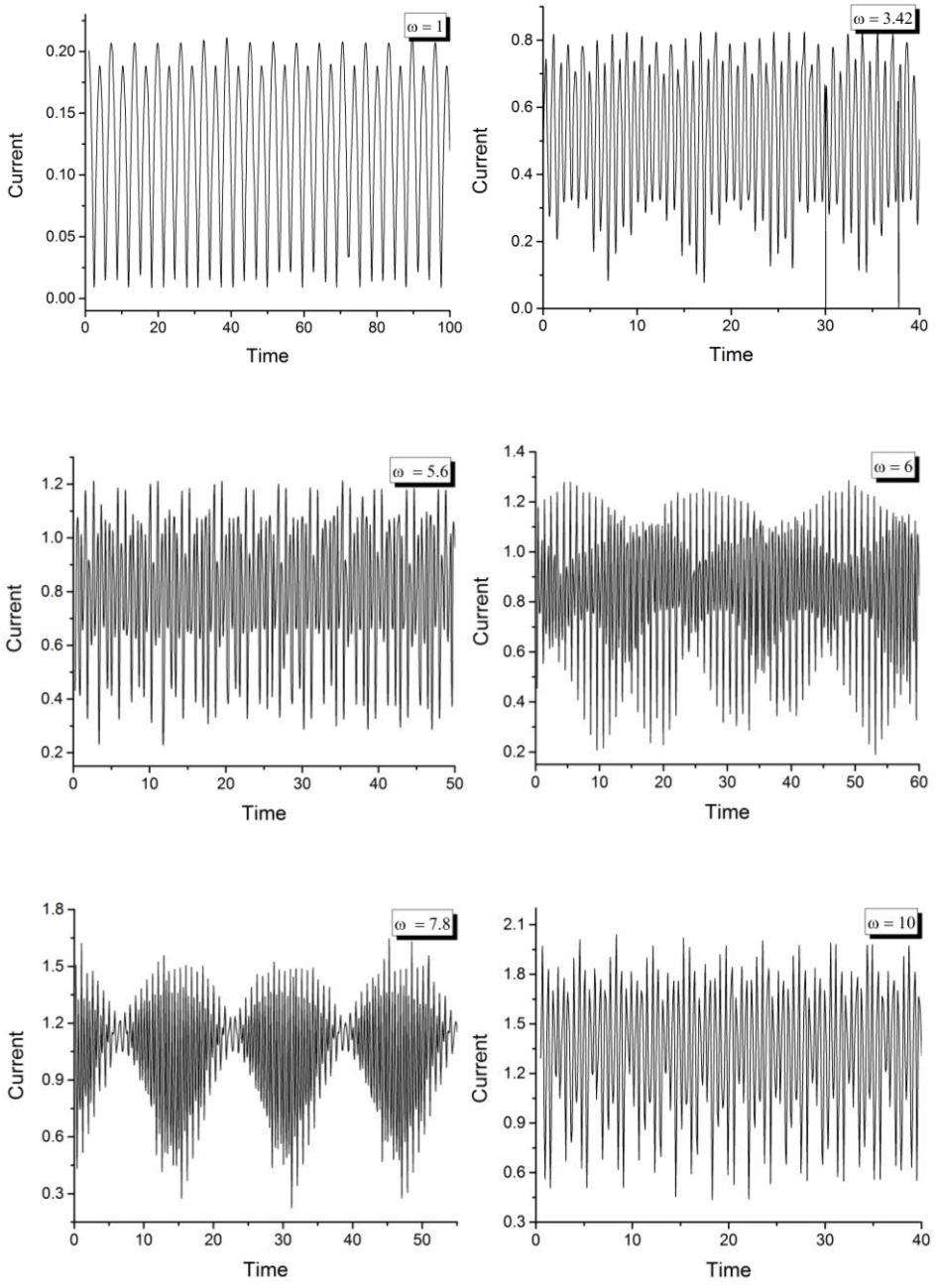

Fig. 3 – Time series of the discharge current obtained from the theoretical model, for different value of ω.

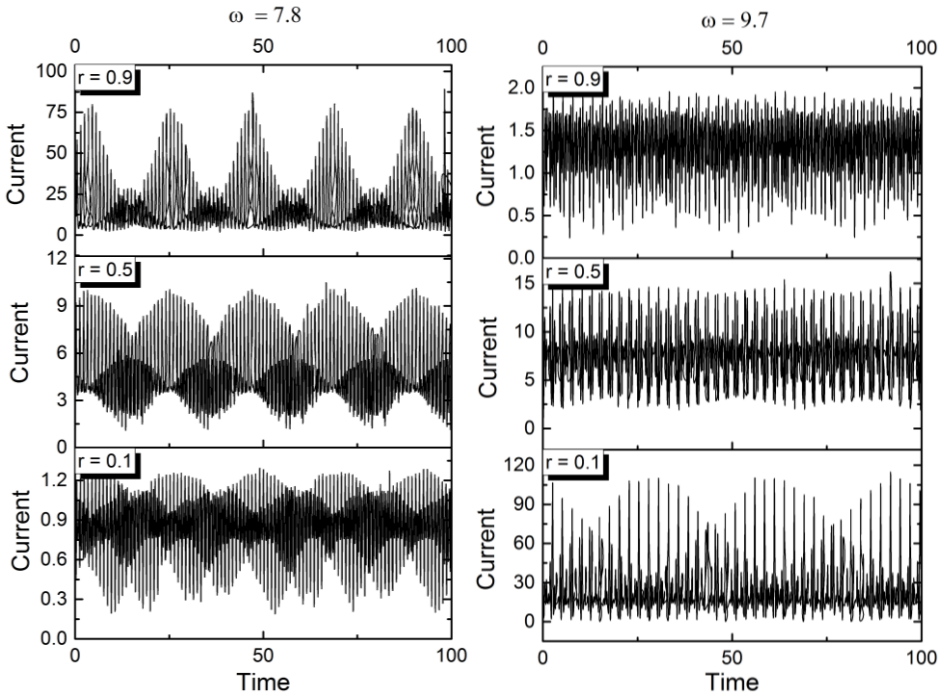

Fig. 4 – Time series of the discharge current obtained from the theoretical model, for different value of *r* and two values of ω.

3. Conclusions

By assuming that the discharge plasma particles moves on continuous but non-differentiable (fractal) curves, a theoretical model was developed in the frame of Scale Relativity Theory, able to explain the phenomenon of self-modulation of the plasma system dynamics. The obtained results from the this theoretical model are in good agreement with the experimentally recorded ones.

REFERENCES

Arnold V.I., *Mathematical Methods of Classical Mechanics*, 2nd Edition, Springer, New York, 1989.

Barnsley M.F., *Fractals Everywhere*, 2nd Edition, Academic Press, Cambridge MA, 1993.

Cariñena J.F., Ramos A., *Riccati Equation, Factorization Method and Shape Invariance*, Rev. Math. Phys. A, **12**, 1279-1304 (2000).

Chen F.F., *Introduction to Plasma Physics and Controlled Fusion*, 3rd Edition, Springer, Heidelberg, 2016.

Denman H.H., *Time-Translation Invariance for Certain Dissipative Classical Systems*, Am. J. Phys., **36**, 516-519 (1968).

Dimitriu D.G., Irimiciuc S.A., Popescu S., Agop M., Ionita C., Schrittwieser R.W., *On the interaction Between Two Fireballs in Low Temperature Plasma*, Phys. Plasmas, **22**, 113511 (2015).

Falconer K., *Fractal Geometry – Mathematical Foundations and Applications*, 3rd Edition, John Wiley & Sons, Chichester UK, 2014.

Hastings H.M., Sugihara G., *Fractals – A User's Guide for the Natural Sciences*, Oxford University Press, 1993.

Hillborn R.C., *Chaos and Nonlinear Dynamics – An Introduction for Scientists and Engineers*, 2nd Edition, Oxford University Press, 2000.

Ioannidou H., *Statistical Interpretation of the Planck Constant and the Uncertainty Relation*, Int. J. Theor. Phys., **22**, 1129-1139 (1983).

Libermann P., Marle C.M., *Symplectic Geometry and Analytical Mechanics*, D. Reidel Publishing Company, Dordrecht, 1987.

Mandelbrot B.B., *The Fractal Geometry of Nature*, W. H. Freeman, New York, 1982.

Merches I., Agop M., *Differentiability and Fractality in Dynamics of Physical Systems*, World Scientific, Singapore, 2016.

Mitchell M., *Complexity – A Guided Tour*, Oxford University Press, 2009.

Morozov A.I., *Introduction to Plasma Dynamics*, CRC Press, Boca Raton FL, 2012.

Nottale L., *Fractal Space-Time and Microphysics – Towards a Theory of Scale Relativity*, World Scientific, Singapore, 1993.

Nottale L., *Scale Relativity and Fractal Space-Time – A New Approach to Unifying Relativity and Quantum Mechanics*, Imperial College Press, London, 2011.

Stoler D., *Equivalence Classes of Minimum Uncertainty Packets*, Phys. Rev. D, **1**, 3217-3219 (1970).

Zelkin M.I., *Control Theory and Optimization I, Encyclopedia of Mathematical Sciences*, **86**, Springer-Verlag, Berlin, 2000.

AUTOMODULAREA DINAMICII UNEI PLASME DE DESCĂRCARE CU CATOD CAVITAR
II. Modelare teoretică

(Rezumat)

Este propus un model teoretic, dezvoltat în cadrul Teoriei Relativității de Scală, capabil să explice automodularea dinamicii unei plasme de descărcare cu catod cavitar. În cadrul acestui model, complexitatea interacțiunilor din volumul de plasmă a fost înlocuită de nediferențiabilitate (fractalitate). Particulele din plasma de descărcare se mișcă liber, fără constrângeri, pe curbe continue dar nediferențiabile, într-un spațiu fractal. S-a obținut o ecuație de tip Riccati, ce descrie dinamica unui oscilator armonic. Soluția acestei ecuații prezintă o modulare a frecvenței prin intermediul unei transformări Stoler. Rezultatele obținute sunt în bună concordanță cu cele experimentale.

BULETINUL INSTITUTULUI POLITEHNIC DIN IAŞI
Publicat de
Universitatea Tehnică „Gheorghe Asachi” din Iaşi
Volumul 63 (67), Numărul 2, 2017
Secţia
MATEMATICĂ. MECANICĂ TEORETICĂ. FIZICĂ

DIMENSIONALITY AND NON-DIFFERENTIABILITY

BY

IRINEL CASIAN BOTEZ*

"Gheorghe Asachi" Technical University of Iaşi,
Faculty of Electronics, Telecomunication and Information Technology

Received: June 16, 2017
Accepted for publication: September 26, 2017

Abstract. Dimensionality is one of principal characteristics that define the material parameters. The same compound can exhibit dramatic different properties depending on whether it is arranger in 1D, 2D or 3D structure. Although quasi-1D (*e.g.* nanotubes), 2D (*e.g.* grapheme) and, of course, 3D physical objects are well documented, dimensionality is conspicuously absent among the theoretical approach. We investigate the link between this dimensionality and the differentiable approach.

Keywords: non-differentiability; fractals.

1. The Theory

The present day physics, since the time of Newton and Leibniz, the founders of the integro-differential calculus, is based on the unjustified assumption of the differentiability of the space-time continuum. We say "unjustified" because there is neither a priori principle nor definite experiments that impose such approach. Moreover, this hypothesis is clearly broken by the quantum mechanical behavior. It was demonstrated by Feynman (Feynman and Hibbs, 1965) that the typical paths of quantum mechanical particles are continuous but non-differentiable.

*Corresponding author; *e-mail*: irinel_casian@yahoo.com

A geometrical intuitive notion of dimension is given by the exponential link between object's bulk and size (a linear distance) (Theiler, 1990):

$$bulk \sim size^{dimension} \tag{1}$$

So, if the space is differentiable, the *dimension* is a constant, the topological dimension of the object, D_T. If the space is continuous but non-differentiable, the *dimension* is different from the topological dimension:

$$dimension = D_T - D_F \tag{2}$$

and the bulk tends to infinity when the size tends to zero, which means, from Eq.(1), that dimension is negative:

$$D_T < D_F \tag{3}$$

Mandelbrot named D_F the *fractal dimension* of the object (Mandelbrot, 1983). In other words, a non-differentiable space-time continuum is necessarily *fractal,* in the general meaning initially given by Mandelbrot (Mandelbrot, 1975; Mandelbrot, 1983).

In such systems implying fractals and non-differentiability, Scale Relativity Theory proposes the introducing of a new frame of thought where all scales co-exist simultaneously as different worlds, but are connected together via scale-differential equations. The quantum behavior may be reinterpreted as a manifestation of scale relativity.

A question is rising: what is the meaning of new differential in respect to scale? We must remember that Lobesgue's theorem (Titchmarsh, 1939) states that: *a continuous curve of finite length is differentiable or almost everywhere differentiable*.

Now let us consider the set of continuous real-valued functions $f(s)$, defined on a compact set I of $\mathbb{R}$. We denote this set by $C^0(I)$ and the subset of continuous and nowhere differentiable on I by $\mathcal{C}^0(I)$. The variable s, proper time, provides the parameterization of the graph, Γ, of the function $f(s)$. The classical way to construct an intrinsic coordinates system on the graph Γ is to introduce the so-called *curvilinear coordinate* as the *length*, $\mathcal{L}(f;s,s_0)$, of the graph Γ between the points $[s_0, f(s_0)]$ and $[s, f(s)]$,

where $s_0 \in I$ is a given origin. If $f(s)$ is non-differentiable, we cannot use such construction because we have the converse of the Lebesgue's theorem: *if* $f(s)$ *is everywere non-differentiable then the length of* $f(s)$ *is infinite.*

In the framework of Scale Relativity Model is introduced a new point of view which is that we can have access:

– not to the function $f(s)$, but to a representation of it (controlled by a resolution constraint ε)

– to the behavior of this representation when this resolution changes.

This representation of the function $f(s)$ is a one-parameter family of real-valued functions, denoted $F(s,\varepsilon)$, $\varepsilon \in \mathbb{R}^+$, which has the properties that;

a) for all $\varepsilon > 0$, the function $F(s,\varepsilon)$ is differentiable;

b) $\lim_{\varepsilon \to 0} F(s,\varepsilon) = f(s)$.

Such functions are named *fractal functions.* Fractal function $F(s,\varepsilon)$ is a function of two variables, s (in space-time) and ε (in scale space). A common fractal function is the length, $\mathcal{L}(s,\varepsilon)$, of the polygonal approximation of the graph Γ of a non-differentiable function, considered between the points $A = A_0[s_0, f(s_0)]$ and $B = [s, f(s)]$.

This length increases monotonically when the resolution ε tends to zero. So the length of the graph of a continuous and almost everywhere non-differentiable function is *scale divergent*.

Therefore, this law of divergence, named scale law, was intensively studied (LeMehaute, 1991; Tricot, 1999; Cresson, 2002). For example, Cresson (Cresson, 2002) defines a *scale variable* as:

$$E = ln\left(\frac{\varepsilon}{\varepsilon_0}\right) \tag{4}$$

where $\varepsilon > 0$ is an absolute resolution described with respect to a given origin of resolution ε_0. In this *scale reference system,* we have $E = 0$ for $\varepsilon = \varepsilon_0$, $E > 0$ for $\varepsilon > \varepsilon_0$ and $E < 0$ for $\varepsilon < \varepsilon_0$.

The scale law (Cresson, 2002) is given by:

$$\frac{d\mathcal{L}(s,E)}{dE} = A(\mathcal{L}) \tag{5}$$

where $A: \mathbb{R} \to \mathbb{R}$. This law describes a relation between the space reference system and the scale reference system. The simplest law corresponds to the first degree polynom:

$$\frac{d\mathcal{L}(s,E)}{dE} = a + b\mathcal{L} \tag{6}$$

with a,b are functions of s in most general case, "a" having the dimension of length and "b" being dimensionless. In our approach we shall consider that $b(s) = b = const.$.

Eq. (6) is an ordinary differential equation of the first order which have the solution:

$$\mathcal{L}(s,E) = -\frac{a(s)}{b} + \left[\frac{a(s)}{b} + \mathcal{L}_0(s)\right] e^{bE} \tag{7}$$

where $\mathcal{L}_0(s) = \mathcal{L}(s,0)$. Eq. (7) can be rewritten as:

$$\mathcal{L}(s,\varepsilon) \approx \mathcal{L}_1(s)\eta(s)\left(\frac{\lambda_0}{\varepsilon}\right)^{-b(s)} \tag{8}$$

In this circumstances, let us remember that, following Mandelbrot (Mandelbrot, 1983), the length of a fractal curve satisfies (Mandelbrot, 1983), page 36, I quote:

$$L(\varepsilon) \approx \varepsilon^{1-D} \tag{9}$$

where D is the *fractal dimension* which describe the dimensional discordance of the fractal sets (in our case the set is the curve). Therefore, if we compare Eq. (8) with Eq. (9), we have:

$$-b(s) = D_F - 1 \tag{10}$$

So Eq. (7) become:

$$\mathcal{L}(s,\varepsilon) = \mathcal{L}_1(s) + \mathcal{L}_1(s)\eta(s)\left(\frac{\lambda_0}{\varepsilon}\right)^{D_F - 1} \tag{11}$$

Let $X(s,\varepsilon)$ be one of the representation of the axes, we have:

$$X(s,\varepsilon) = x(s) + x(s)\eta_x(s)\left(\frac{\lambda_0}{\varepsilon}\right)^{D_F-1} \tag{12}$$

In the simplest case, we have to restrict to the case of self-similar fractal curves which have constant fractal dimension.

2. Conclusions

The main conclusions of this paper is that first consequence of the reducing dimensionality is the non-differentiability (fractality) of space-time. In such situation we can use a representation of the non-differentiable quantity which will depend compulsory of resolution.

REFERENCES

Cresson J., *Scale Relativity Theory for One-Dimensional Non-Differentiable Manifolds*, Chaos Solitons & Fractals, **14**, *4*, 553-562 (2002).

Feynman R., Hibbs A., *Quantum Mechanics and Path Integrals*, New York, McGraw-Hill (1965).

LeMehaute A., *Fractal Geometries*, Boca Raton, CRC Press (1991).

Mandelbrot B.B., *Les Objets Fractales*, Paris, Flammarion (1975).

Mandelbrot B.B., *The Fractal Geometry of Nature*, New York, W.H. Freeman and Company (1983).

Theiler J., *Estimating Fractal Dimension*, J. Opt. Soc. Am. A, **7**, *6*, 1055-1073 (1990).

Titchmarsh E.C., *The Theory of Functions*, London, Oxford University Press (1939).

Tricot C., *Curbes et Dimension Fractale*, Berlin, Springer-Verlag (1999).

DIMENSIONALITATE ŞI NON-DIFERENŢIABILITATE

(Rezumat)

Dimensionalitatea este una dintre principalele caracteristici care definesc parametrii materialului. Acelaşi compus poate prezenta în mod dramatic diferite proprietăţi, în funcţie de faptul dacă este aranjat în structură 1D, 2D sau 3D. Deşi obiectele cvasi-1D (de ex., Nanotuburile), 2D (de exemplu, grafimele) şi, desigur, obiectele fizice 3D sunt bine documentate, dimensionalitatea este absentă în mod vizibil în abordarea teoretică. Investigăm legătura dintre această dimensionalitate şi abordarea diferenţiată.

BULETINUL INSTITUTULUI POLITEHNIC DIN IAŞI
Publicat de
Universitatea Tehnică „Gheorghe Asachi” din Iaşi
Volumul 63 (67), Numărul 2, 2017
Secţia
MATEMATICĂ. MECANICĂ TEORETICĂ. FIZICĂ

AN OVERVIEW OF REMOTE SENSING TECHNIQUES FOR THE TROPOSPHERIC AEROSOLS MONITORING. A CASE STUDY

BY

MARIUS MIHAI CAZACU[1,2,*], OVIDIU GELU TUDOSE[3], OANA RUSU[2], ADINA ELENA SCRIPA (TUDOSE)[4] and IRINA RADINSCHI[1]

[1]“Gheorghe Asachi” Technical University of Iași,
Department of Physics
[2]“Alexandru Ioan Cuza” University of Iași,
Faculty of Physics, Atmosphere Optics, Spectroscopy and Lasers Laboratory
[3]SC INOESY SRL, Iași
[4]“Alexandru Ioan Cuza” University of Iași,
Faculty of Physics

Received: August 28, 2017
Accepted for publication: September 26, 2017

Abstract. In what manner weather parameters vary in time and space, a single point measurement provides information for a local and a small area. Thus, a network of monitoring systems is beneficial both for weather forecasts, accurate determination of input parameters in models dispersion of pollutants and atmospheric studies for a large area so that the data collected can be used for a statistical analysis and optimization and validation of models, as. In this context, from 2010, a new lidar network at a national level was initiated under the development in the framework of Romanian LIdar NETwork (ROLINET) research project. One year later, the Romanian Atmospheric 3D research Observatory – RADO was founded. By correlating laboratory data with on-site measurements performed over several measurement campaigns (measurements performed from the ground level up to 15-20 km altitude), modern remote

[*]Corresponding author; *e-mail*: marius.cazacu@tuiasi.ro

sensing techniques used at a national level and recently results will be presented in this paper.

Keywords: lidar; sun-photometer; AERONET; Saharan dust; aerosols.

1. Introduction

Climate warming is predominantly caused by greenhouse gases and manifests itself at a global scale, while local atmospheric cooling is regionally experienced in the vicinity of industrial sites, as an example. Atmospheric aerosols typically cause this regional effect cooling. The last report of the Intergovernmental Panel on Climate Change – IPCC, 2013, indicates that the contribution of tropospheric aerosols over the total heat exchange balance (Earth-space) is not entirely known (IPCC, 2013). In Fig. 1 can be observed the aggregated uncertainties for the main drivers of climate change and contribution to the net radiative forcing. As can be seen, the cloud adjustments due to aerosols have a low value for the level of confidence.

Understanding the contribution of atmospheric aerosols to Earth's radiative equilibrium, improved climate predictive computer models may emerge, enhancing the impact of global warming. Poly-cycle aromatic hydrocarbons and soot emitted by incomplete combustion burning, part of atmospheric aerosols are of highly significant scientific attention since they may produce complex physico-chemical processes in the local atmosphere leading to weather/climatic variations.

The study of different physico-chemical processes in atmosphere having as catalysts aerosols is both done in the laboratory and onsite. In laboratory experimentation, the interaction of various chemical compounds adsorbed on the surface of micro-particles of soot, ice or/and others can be studied. Some of the effects can include carcinogenic effects (IPCC, 2013).

Firstly, the aerosol is a system of particles (liquids, solids) suspended in a gaseous environment long enough to be observed and characterized. In the gaseous atmospheric environment it is standard practice to include all solid and liquid particles, excepting the hydrometeors (water droplets, ice crystals) (Fucic *et al*., 2012).

According to size, the atmospheric aerosols have a large range, from nanometric particles (a couple of molecules) to particles greater than ten μm. Aerosols influence the ambient air quality and visibility. The heat balance received by Earth's crust directly by reflecting the solar radiation back into space and indirectly by variation of absorption and reflection coefficients of the cloud formations (Stefan *et al*., 2008). Similarly, aerosols can act as catalysts for chemical reactions (*i.e.*, chemical reactions leading to the ozone layer thinning) (Seinfeld and Pandis, 2006; Stefan *et al*., 2008).

Therefore, vertically measurements of physical and optical parameters of the aerosols are still of great interest. The vertically monitoring of regional air pollution to complement the ground-based stations is nowadays clearly confirmed both by the key information regarding the atmospheric aerosols dynamics (as PBL height (Planetary Boundary Layer) and its variability) and the regional or long-range transport of aerosols load estimation. The interaction between the aerosols (regional to global) as a trigger of local pollution and meteorology (*i.e.*, extreme events) is still not well known and difficult to assess without high-resolution fast atmospheric information (Shon *et al*., 2008).

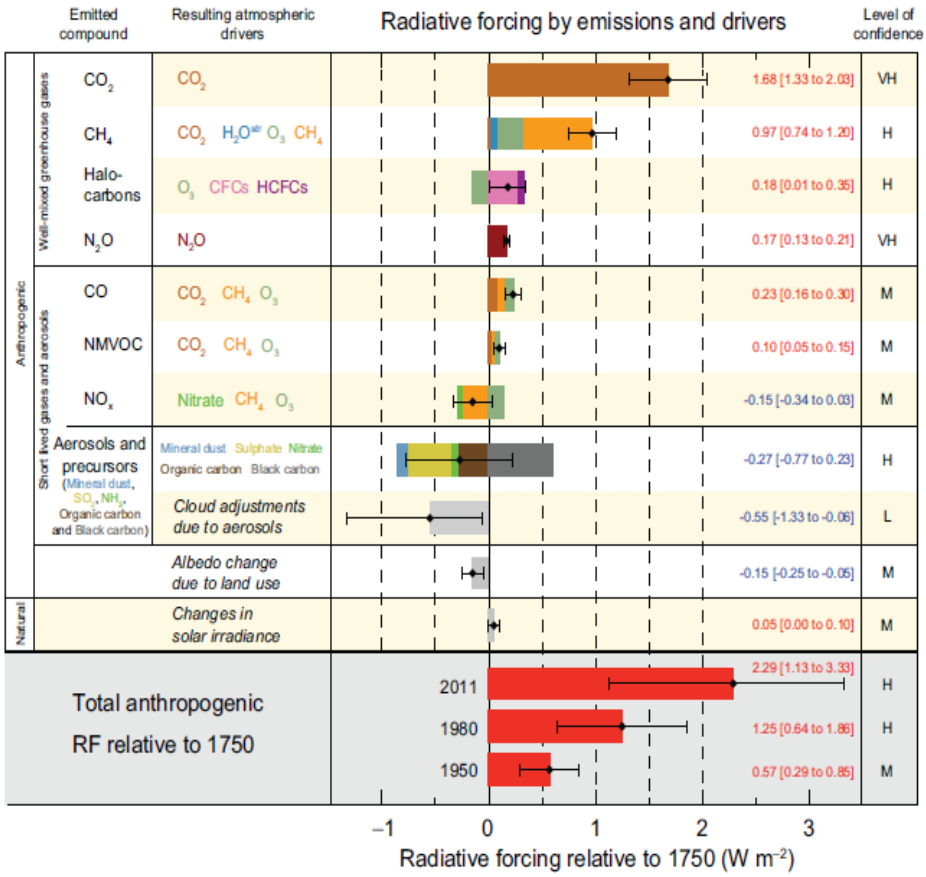

Fig. 1 – Radiative forcing estimates in 2011 relative to 1750 and uncertainties for the main drivers of climate change, after (IPCC, 2013).

Based on this approach, a significant breakthrough by continuous expansion and networking of remote sensing ground is given by developing of GAW program (Global Aerosol Watch Program) for solar photometry such as AERONET (AEerosol Robotic NETwork), and lidar systems (Light Detection

and Ranging) for instance: EARLINET, Asian Dust network (ADNET), Micro-Pulse Lidar network (MPLNET) ALINE - Latin America or CISLINET Lidar network (lidar network in the former USSR) (IPCC, 2013).

At national level, RADO is a distributed atmospheric research infrastructure based on the partnership between: National Institute of R&D for Optoelectronics, "Alexandru Ioan Cuza" University of Iasi, "Babes-Bolyai" University of Cluj-Napoca, University of Bucharest and National Administration for Meteorology (Cazacu *et al*., 2012; Holben *et al*., 1998; Mattis, 2004; "RADO - Romanian Atmospheric 3D research Observatory", 2015; Welton *et al*., 2001). Numerous coordinated experimental campaigns within Observation Network that is based on 5 existing lidar stations, which operate as the ROLINET, occurred (Cazacu *et al*., 2012; Papayannis *et al.*, 2014; Timofte *et al*., 2011). Four of them are equipped with elastic backscatter lidars, with a dynamic range from 500 m to 15 km and a spatial resolution of 3.75 m and a multiwavelength Raman lidar (3 elastics + 2 Nitrogen Raman + 1 water vapor channel) that is used at the INOE coordinator site, along with a tropospheric ozone lidar. All stations operate AERONET (Aerosol Robotic Network) sunphotometers and ground-level in situ instruments, such as particle counters, gas analyzers and weather stations (Cazacu *et al*., 2012; Papayannis *et al*., 2014; Timofte *et al.*, 2011).

2. The Lidar Technique

In 1930, E.H. Synge (Stefan *et al*., 2008) proposed a method to characterize the atmospheric density by scattering the light beam. In 1963, Smullins and Fiocco used for the first time the lidar system with a Ruby laser as a light source (694 nm and energy/pulse ratio of 0.5 J) (Stefan *et al*., 2008).

A lidar system working on the same principle as a radar. The main difference is that the source of radiation is a pulsed laser beam. The wavelength of a lidar system is selected accordingly to the atmospheric components to be investigated, and it can be varied between 355 nm up to 1064 nm (covering the UV – VIS- IR spectrum) (Fiocco and Smullin, 1963).

The fluorescence, absorption, elastic scattering and inelastic scattering occurring due to the interactions between pulsed laser radiation and atmospheric constituents. Backscattered electromagnetic radiation captured by the detection system of the lidar contains information about the beam laser and aerosols interaction. Additional studies are necessary to separate and weight the contribution of each observed phenomenon to the total possibilities of matter/laser interaction.

The lidar system consists of an emission module (including the laser source and the beam expander), a reception module (including among others a telescope, lenses, wavelength filters and photomultipliers) and an acquisition

system. The lidar system is configurable to work based on several light-matter interactions, thus allowing studying different physical processes (Fig. 2).

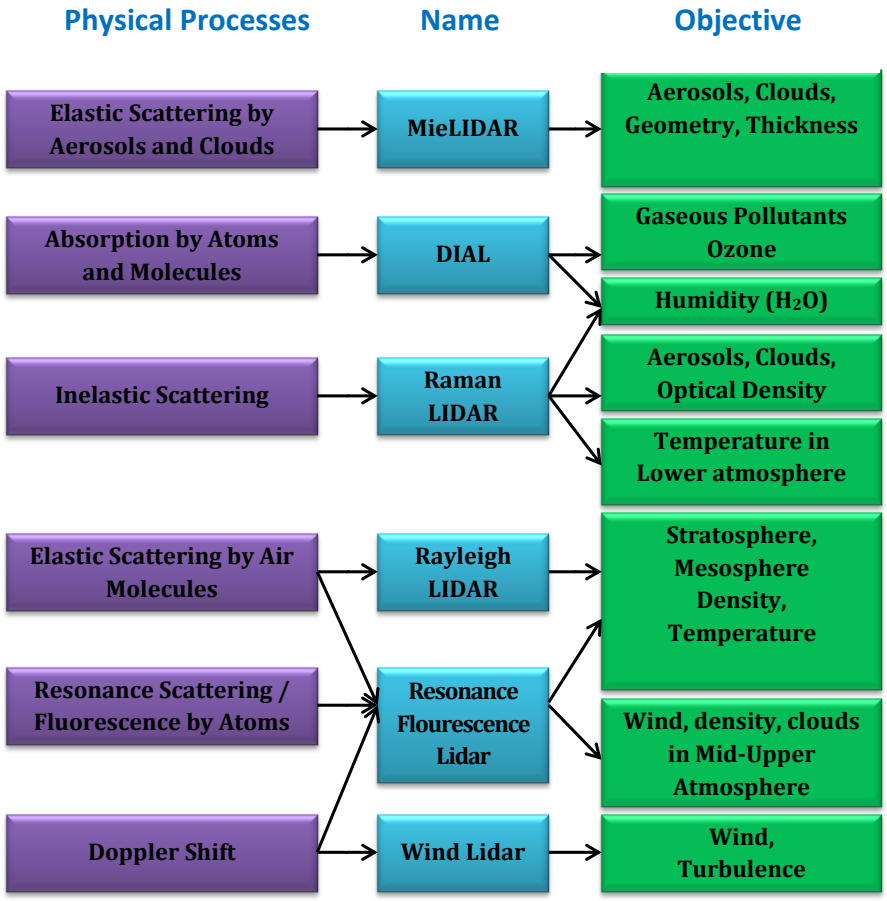

Fig. 2 – Types of Lidar systems.

The new ^{ESY}LIDAR system designed as being a modular system, mobile, easy technically upgradable (multi-angle, multi-channel) for various applications, is used at the Iaşi, Cluj-Napoca and Timişoara monitoring sites. The first version was based on a coaxial UV (355 nm), VIS (532 nm) and NIR (1064 nm) emission of a Nd:YAG laser with a variable repetition rate up to 30 Hz. The divergence of the 6 mm laser beam of 0.75 mrad was five times improved, by using a 3λ beam expander resulting in a beam of 30 mm diameter and a final divergence of 0.15 mrad (Measures, 1984). This lidar transmitter offers the possibility to perform measurements up to high altitudes up to 12 km during daytime and as high as 15 km during nighttime for just one minute

integration time and keeping an extremely high resolution as 3.76 m for example (Cazacu, 2010).

The [ESY]LIDAR receiver is based on a Newtonian telescope being equipped with a 406 mm diameter of primary mirror and a focal length of 1829 mm.

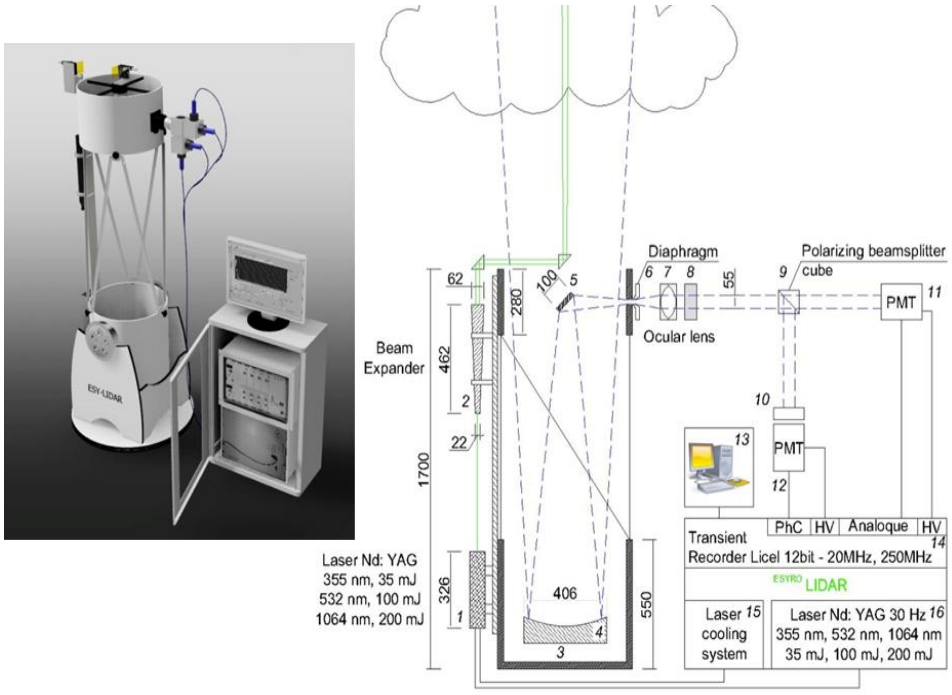

Fig. 3 – Schematic overview of the [ESY]Lidar system:
1. Nd: YAG Laser, 2. Beam expander, 3. The Newtonian telescope, 4. Main mirror, 5. Secondary mirror, 6. Diaphragm, 7. Eye-piece, 8. Interference filters, 9. Polarizing beamsplitter cube, 10. Optical filter, 11. Photomultiplier (in analog regime), 12. Photomultiplier (in photon-counting mode), 13. Computer for data analysis, 14. Acquisition board, and analog to digital converter 15. Laser cooling unit, 16. Laser power supply (Tudose *et al*., 2011).

The detection module is supplementary equipped with a lens system, filters and diaphragms which limit the acceptable spectrum, focus and select the reflected spectrum reaching the photomultipliers to make the most out of the useful signal produces by the laser-matter interaction (Tudose *et al*., 2015). The improved version of this lidar system proposed by Tudose *et al*. was firstly based using the matrix formalism (Cazacu, 2010; Tudose, 2013). All resulting optical parameters were used in the final technical configuration of the on-axis lidar system that is represented in Fig. 3.

The upgraded version was initiated to improve the fixation/alignment system by decreasing the distance between the optical axis of the emission module and the telescope (from the 360 mm to 320 mm). Thus, this reduced distance changes the overlap factor, which describes the overlapping radiation ratio at emission and reception. According to previous works, the overlapping factor is of uttermost importance since is a constant in the lidar equations (Tudose *et al*., 2015).

A LabVIEW code developed by Talianu based both on the equations described by specialized literature and on the geometric optics specifications of the lidar system is used to calculate the overlapping factor (Cazacu, 2010; Measures, 1984; Nemuc *et al*., 2013; Nicolae *et al*., 2010; Tudose *et al*., 2011). As further modeling parameters, the overlapping factor is computed depending on the distance between the optical axis, and the declination angle between axes for a given optimal configuration at which the lidar signal is acquired.

The maximum value (the entire laser beam enters the field of view of the telescope) is achieved at an altitude of about 750 m by computing the overlapping factor using the values gives in Table 1, (in the standard configuration) (Ciobanu *et al*., 2003; Harms *et al*., 1978; Measures, 1984; Stefan *et al*., 2008; Talianu, 2008) and 700 m (in the upgraded configuration) (Cazacu, 2010; Tudose *et al*., 2011), see Fig. 4.

Table 1

Technical Parameters Used for Computing the Overlapping Factor

Parameter	ESY Lidar – standard configuration	ESY Lidar – upgraded configuration
Laser pulse energy, [mJ]	100	
Telescope object diameter, [mm]	40	
Multiplication factor of the laser beam expander	5x	
Initial laser divergence, [mrad]	0.75	
Distance between axis, [mm]	360	320
Diameter of the Diaphragm aperture, [mm]	11	
Declination angle between axis, [mrad]	0.45	0.43

The diaphragm aperture can be reduced during the sunny days (necessary to maintain a good signal to noise ratio) and to maintain the photomultipliers in the linear response region for the specific wavelength. By varying the aperture, the overlap factor is changing. In case of an aperture diameter variation (from 12 mm to 3 mm), the declination angle has to be

changed from -0.5 mrad to 0.35 mrad thus the altitude where the overlapping factor becomes 1 (the maximum value) can vary between 700 m and 950 m.

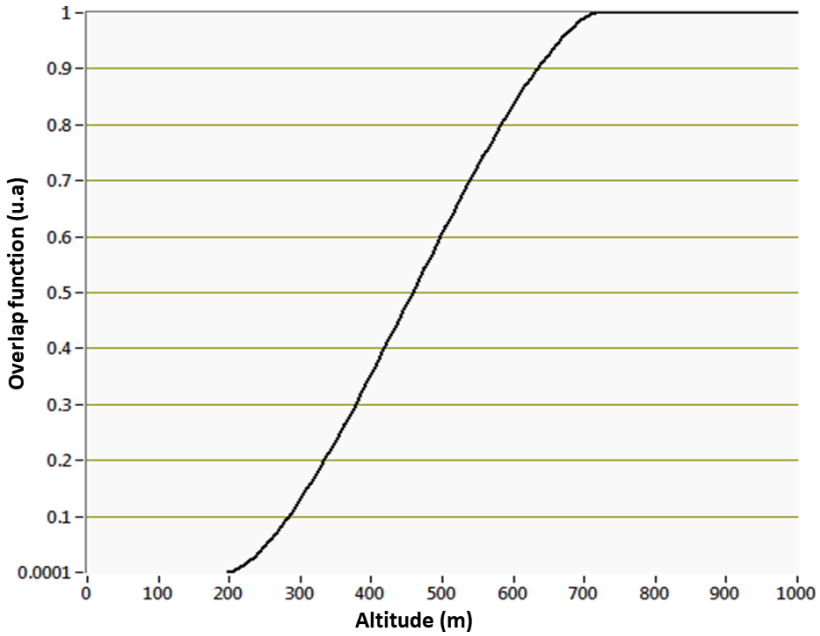

Fig. 4 – The overlap function of the [ESY]Lidar system.

3. Experimental and Computational Methods Used to Optimize the Data Acquisition of Lidar Signals. A Case Study

The lidar signal arriving at the acquisition board is an electrical signal emerging from the conversion of light by photomultipliers located in the detection module. The characteristics of this electrical signal contain all the relevant information resulted from the laser-atmosphere interaction. Any source of measurement errors must be accounted for, and reduced if possible. The largest contributions to measurement errors are the background radiation and the dark current (Tudose, 2013; Tudose *et al.*, 2015). Other noise source is the electronic noise (thermic noise, 1/f noise and impulse noise).

Fig. 5 indicates a raw lidar signal (532 nm, analog mode). To this raw signal, correction and optimization methods was applied. The amplitude of the backscattered signal varies with the altitude. At the upper the altitude, the collected amplitude of the signal is reduced. The Range Corrected Signal (RCS) is defined as the product between the lidar signal (signal amplitude in mV or MHz) and the distance squared (due to the solid angle).

The RCS profile is shown in Fig. 6 and it can indicate the various atmospheric layers. Thus, the raw data can be presented as time series, one by one, as can be show in Fig. 7.

For accuracy, the dark current/noise created by electronic components, before any set of atmospheric measurements, 5 min run and record of noise must be performed. The lidar system will have the main optical mirror closed and the photomultipliers will not collect any photons.

Electronic oscillations (easily observable in fast lidar measurements) are caused by electronic noise from: the triggering system, the reflections from the near vicinity of the telescope and from the lidar signal arriving from various sources located along the laser beam path (*e.g.* clouds).

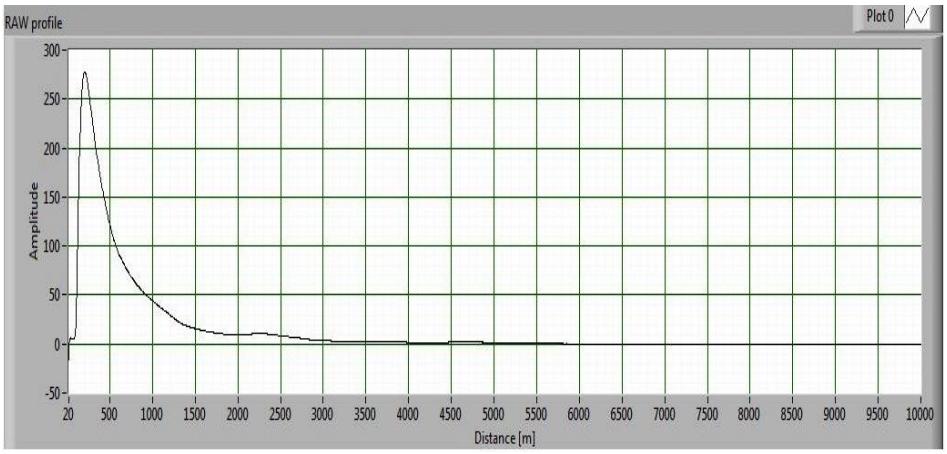

Fig. 5 – Raw lidar signal.

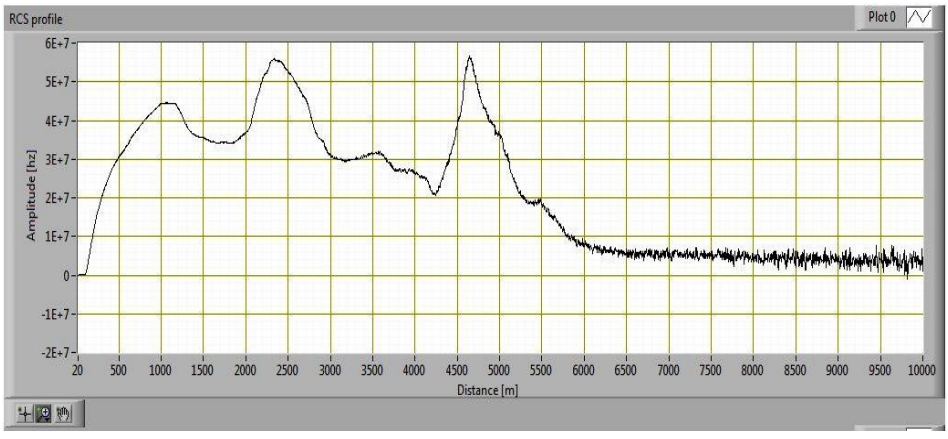

Fig. 6 – Range corrected signal lidar (29.05.2013, 20.40 – 21.00 LT).

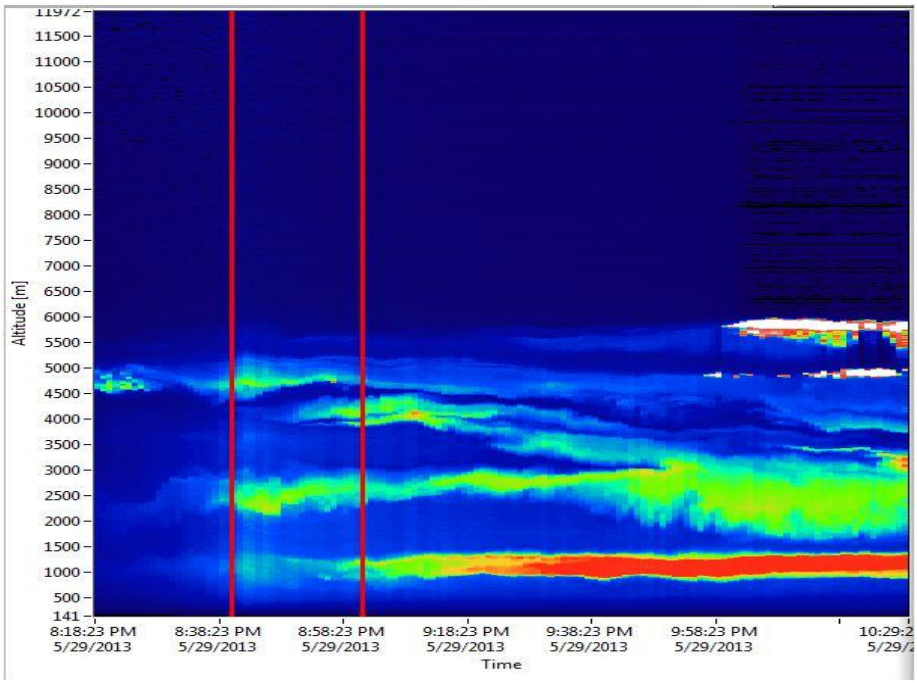

Fig. 7 – lidar – range corrected signal time series of raw data [RCS], 29.05.2013, 20.40 – 21.00 local time.

To reduce this effect, the detection module (Licel) is used. The module is optimized to work with lidar signals of up to 500 mV. Neutral optical filters can be used if stronger lidar signals are required (in the Volt range). As an example, the intense peak in amplitude is caused by a secondary reflection of the laser beam in the proximity of the telescope observable in Fig. 8.

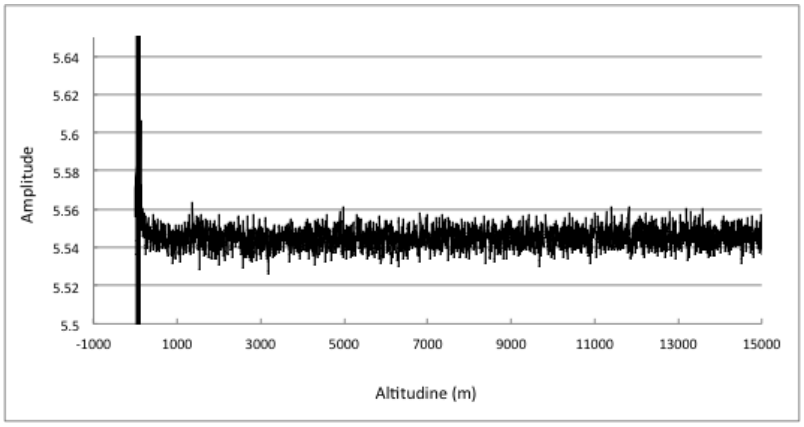

Fig. 8 – The dark current/noise measurement (29.05.2013, 21.00 LT).

Typically, the lidar data are correlated with complementary techniques such as the AERONET sunphotometers, the Calipso lidar system, and with theoretical models (DREAM, HYSPLIT). AErosol RObotic NETwork (AERONET) is a NASA network for monitoring and characterizing atmospheric aerosols by ground-based sun photometer. Beginning with the 7th of May 2013, the monitoring station LOA-SL in Iași, Romania (47.19306° North, 27.55556° East) is active in this network providing quantitative values for various types of aerosols (Measures, 1984; Stefan *et al*., 2008). A sun-photometer absorb direct the sunlight energy and convert the intensity into a quantified voltage to measure aerosols loading in the atmosphere. The solar irradiance on the top of the Earth atmosphere is constant. The sunlight travels through the atmosphere, while aerosols can dissipate the energy by scattering (Rayleigh) and absorbing the light. Loads of aerosols in the troposhere cause more scattering of the electromagnetic solar radiation. Knowing the thickness of the air column and the spectral irradiance of the sunlight transmitted up to the Earth's surface can allow us to determine the optical properties of different aerosol types (Unga *et al*., 2013).

BSC DREAM Model is an operational website developed by Earth Sciences Division of the Barcelona Supercomputing Center and was used to confirm the presence of Saharan dust over Romania (Basart *et al*., 2012; Cazacu *et al*., 2015; Dubovik *et al*., 2002). Hybrid Single-Particle Lagrangian Integrated Trajectory (HYSPLIT) model is a complete system for computing both simple air trajectories and complex dispersion also with capabilities of deposition simulations (Draxler and Rolph, 2015). The model uses the existing meteorological forecast fields from regional of global models to compute advection, stability and subsequent dispersion (Basart *et al*., 2012; Pérez *et al.*, 2006). The Cloud Aerosol lidar with orthogonal Polarization (CALIOP) system, which is on board of the CALIPSO platform is a three-channel elastic backscatter lidar used for aerosols and cloud investigation. CALIOP is providing level 1 products, thus high-resolution profiles of the attenuated backscatter by aerosols and clouds at visible and near-infrared wavelengths and depolarized backscatter using the visible channels. With algorithms previous developed (Draxler and Rolph, 2015), level 2 products (classification of different features by layer type, *e.g*. clouds *vs*. aerosols, the extinction coefficient profile and total column Aerosols Optical Depth (AOD) for a defined lidar ratio for each detected aerosol layer) are estimated. Mamouri *et al*. and Pappalardo *et al*. have shown that using level 1 for attenuated backscatter profiles are in reasonable agreement with ground-based lidar measurements (Winker *et al*., 2009).

It is well known that the Saharan dust influences the radiative heat transfer via absorption, scattering or reflection, a net change in the energetic flux and solar wavelength reaching the ground is expected. According to literature, atmospheric photosynthesis processes are also altered (Mamouri *et al*., 2009; Pappalardo *et al*., 2010). The presence of Saharan dust can be

indicated by data collected with solar photometry and from the theoretical models of aerosols dispersion.

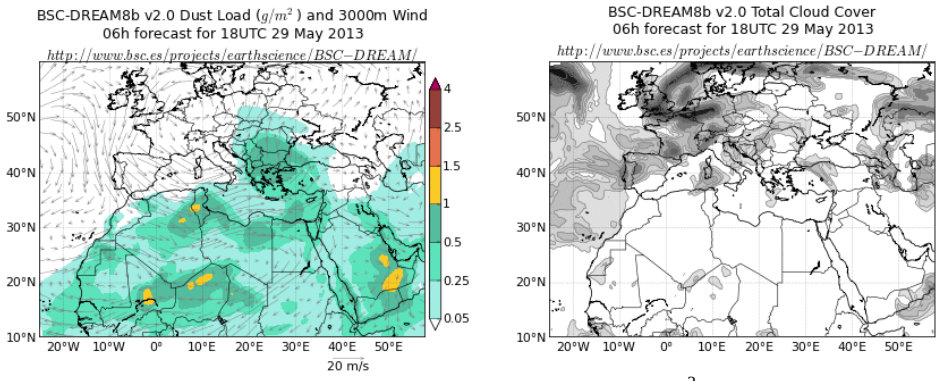

Fig. 9 – The DREAM model - forecast for the amount of dust (g/m^2) and wind (at 3000 m), the image on the left and the forecast for cloud, on May 29, 2013 h18 UT.

On May 29, 2013 during a Saharan dust intrusion event in enough concentrations was forecasted by DREAM model, as is showed in Fig. 9. To highlight the Saharan dust intrusion over Romania, respectively over the Iași city, in collaboration between the Laboratory of Atmospheric Optics Spectroscopy and Lasers (Lat: 47.19306° N Long: 27.55556° W, Elev: 175.0 m) part of Romanian Atmospheric 3D Observatory (RADO) and Enviroscopy SRL some measurements were performed (Ohde and Siegel, 2012).

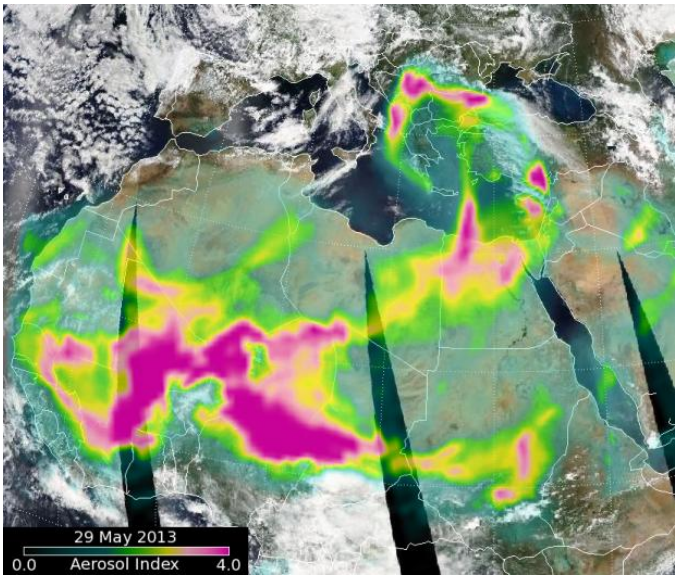

Fig. 10 – Aerosol Index for 29 May 2013 – Aqua MODIS image.

As it is reported in Fig. 10, it can be seen the RGB image on 29 of May 2013 on the EarthObservatory website from the Terra MODIS tool showing a dust plume blowing off the Sahara, across the Mediterranean Sea, and over to Greece and southern Europe.

Lidar data reported by Tudose *et al*., was used from measurements on the night of 29/30 May 2013 (Tudose *et al*., 2013). In the same time, monitoring of the aerosol via satellite imagery was made by using the RGB product (IR8.7 channels, IR10.8 and IR12.0) dedicated to dust detection. The RCS time series from lidar data and HYPLIT backward trajectories confirm the presence of Saharan dust at altitudes of about 2000 m up to respectively 5000 m (Fig. 11).

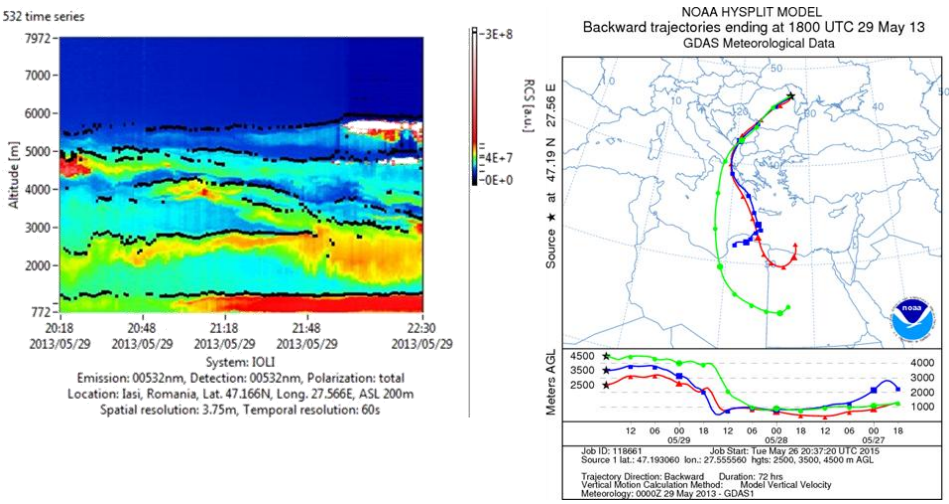

Fig. 11 – Processed RCS time series from 29.05.2013 – local time (left); HYSPLIT backward trajectories form 29 May 2013 (right).

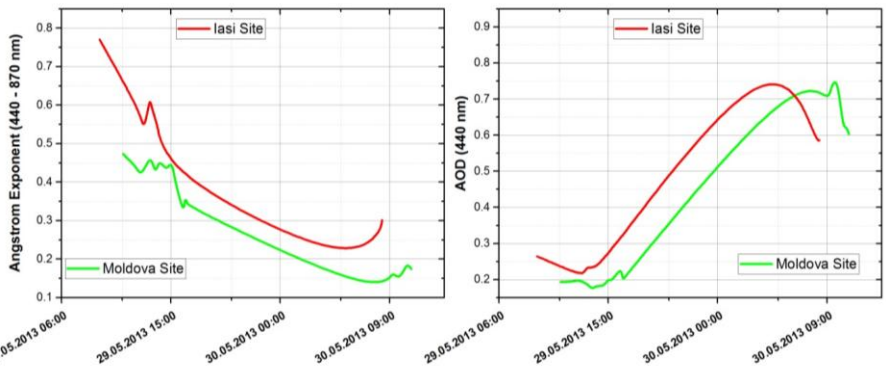

Fig. 12 – Variation of Angstrom exponent (left) and variation of Aerosol Optical Depth (AOD) parameter (right) from 29.05.2013 to 30.05.2013.

Using AERONET Direct sun products it can be observed that during of the 29.05.2013 on LOA-SL_IASI site, urban and industrial aerosols type is predominating with influences of Saharan/mineral dust. These influences are shown in the Fig. 12 and can be identified from complementary studies such as LIDAR data and HYSPLIT models (Tudose *et al*., 2015). While taking into account the main optical parameters like AOD (440 nm) and Ångström Exponent (α(440 – 870 nm)), a preliminary aerosols classification can be achieved. Cazacu *et al.* demonstrated that urban/industrial aerosols have a strong influence over entire aerosols load at LOASL_Iasi site (Nemuc *et al*., 2009; Nicolae *et al*., 2012, 2008). For urban/industrial aerosols $\alpha = 1.2 \div 1.7$ and for dust/ mineral type $\alpha = 0.1 \div 0.8$ according with the scientific literature (Cazacu *et al*., 2015).

3. Conclusions

The modern remote sensing techniques and models was used to describe a case study regarding the classification and environmental impact of the Saharan dust transport on long distances and furthermore to check the possible influences on the local area. The month of May 2013 was chosen as short example, 29th and 30th May, in order to correlate the AERONET data with LIDAR data measurements and the Lagrangian model HYSPLIT confirming the presence of the dust intrusion over urban/industrial aerosols load. Thus, the remote sensing devices must be interconnected and used in correlation to models. Individually, for instance, the information given only by lidar systems are not adequate to completely characterize the aerosols optical properties, especially to properly classifying the aerosols type.

As an immediate perspective, all of these monitoring techniques must be upgraded to the ACTRIS standards both for operational and research measurements [ACTRIS is the European Research Infrastructure for the observation of Aerosol, Clouds, and Trace gases - http://actris2.nilu.no/].

Acknowledgements. This work was supported by the Romanian Space Agency (ROSA) within Space Technology and Advanced Research (STAR) Program (Project no.: 114/7.11.2016 and Project no.: 162/20.07.2017).

REFERENCES

Basart S., Pérez C., Nickovic S., Cuevas E., Baldasano J.M., *Development and Evaluation of the BSC-DREAM8b Dust Regional Model over Northern Africa, the Mediterranean and the Middle East*, Tellus B, **64** (2012), doi:10.3402/tellusb.v64i0.18539.

Cazacu M.M., *Contributions to the Implementation of the First National LIDAR Network for Atmospheric Aerosols Optical Characterization*, PhD Thesis, Alexandru Ioan Cuza University of Iași, Romania (2010).

Cazacu M.M., Timofte A., Talianu C., Nicolae D., Danila M.N., Unga F., Dimitriu D.G., Gurlui S., *Grimsvotn Volcano: Atmospheric Volcanic Ash Cloud Investigations, Modelling-Forecast and Experimental Environmental Approach Upon the Romanian Area*, J. Optoelectron. Adv. Mater., **14**, *5-6*, 517-522 (2012).

Cazacu M.M., Timofte A., Unga F., Albina B., Gurlui S., *AERONET Data Investigation of the Aerosol Mixtures over Iasi area, One-Year Time Scale Overview*, J. Quant. Spectrosc. Radiat. Transf., **153**, 57-64 (2015), doi:10.1016/j.jqsrt.2014.09.004

Ciobanu A., Babin V., Nicolae D., Talianu C., *Numerical Simulations of the Backscattering from a Crystalline Lattice*, J. Optoelectron. Adv. Mater. (2003).

Draxler R.R., Rolph G.D., *HYSPLIT (HYbrid Single-Particle Lagrangian Integrated Trajectory) Model Access via NOAA ARL READY Website [WWW Document]*, NOAA Air Resour. Lab. Silver Spring, MD (2015) URL http://ready.arl.noaa.gov/HYSPLIT.php.

Dubovik O., Holben B., Eck T.F., Smirnov A., Kaufman Y.J., King M.D., Tanré D., Slutsker I., *Variability of Absorption and Optical Properties of Key Aerosol Types Observed in Worldwide Locations*, J. Atmos. Sci., **59**, *3*, 590-608 (2002), doi:10.1175/1520-0469(2002)059<0590:VOAAOP>2.0.CO;2.

Fiocco G., Smullin L.D., *Detection of Scattering Layers in the Upper Atmosphere (60–140 km) by Optical Radar*, Nature, **199**, *4900*, 1275-1276 (1963), doi:10.1038/1991275a0.

Fucic A., Gamulin M., Ferencic Z., Katic J., Krayer von Krauss M., Bartonova A., Merlo D.F., *Environmental Exposure to Xenoestrogens and Oestrogen Related Cancers: Reproductive System, Breast, Lung, Kidney, Pancreas, and Brain*, Environ. Health **11 Suppl 1**, S8 (2012), doi:10.1186/1476-069X-11-S1-S8.

Harms J., Lahmann W., Weitkamp C., *Geometrical Compression of Lidar Return Signals.*, Appl. Opt. **17**, *7*, 1131-1135 (1978), doi:10.1364/AO.17.001131.

Holben B.N., Eck T.F., Slutsker I., Tanré D., Buis J.P., Setzer A., Vermote E., Reagan J.A., Kaufman Y.J., Nakajima T., Lavenu F., Jankowiak I., Smirnov A., *AERONET—A Federated Instrument Network and Data Archive for Aerosol Characterization*, Remote Sens. Environ., **66**, *1*, 1-16 (1998), doi:10.1016/S0034-4257(98)00031-5.

Mamouri R.E., Amiridis V., Papayannis A., Giannakaki E., Tsaknakis G., Balis D.S., *Validation of CALIPSO Space-Borne-Derived Attenuated Backscatter Coefficient Profiles Using a Ground-Based Lidar in Athens, Greece*, Atmos. Meas. Tech., **2**, *2*, 513-522 (2009), doi:10.5194/amt-2-513-2009.

Mattis I., *Multiyear Aerosol Observations with Dual-Wavelength Raman Lidar in the Framework of EARLINET*, J. Geophys. Res., **109**, *D13*, D13203 (2004). doi:10.1029/2004JD004600.

Measures R.M., *Laser Remote Sensing: Fundamentals and Applications*, in: New York, Wiley-Interscience (1984).

Nemuc A., Nicolae D., Talianu C., *Dynamic of the Lower Troposphere from Multiwavelength LIDAR Measurements*, Rom. Reports Phys., **61**, 313-323 (2009).

Nemuc A., Vasilescu J., Talianu C., Belegante L., Nicolae D., *Assessment of Aerosol's Mass Concentrations from Measured Linear Particle Depolarization Ratio*

(Vertically Resolved) and Simulations, Atmos. Meas. Tech. **6**, *11*, 3243-3255 (2013), doi:10.5194/amt-6-3243-2013.

Nicolae D., Belegante L., Nemuc A., *Laser Remote Sensing in Atmosphere Investigation*, Optoelectron. Adv. Mater. – Rapid Commun., **4**, *12*, 1946-1951 (2010).

Nicolae D., Talianu C., Mamouri R.E., Carstea E., Papayannis A., Tsaknakis G., *Air Mass Modification Processes Over the Balkans Area Detected by Aerosol LIDAR Techniques*, J. Optoelectron. Adv. Mater. – Rapid Commun., **2**, 405-412 (2008).

Nicolae D., Vasilescu J., Carstea E., *Estimation of Mass Concentration Profiles for 2-Components External Mixtures of Aerosols, Based on Multi-Wavelength Depolarization Lidar*, in: Proceedings of the 9th International Symposium on Tropospheric Profiling, Session C, ISBN/EAN:978-90-815839-4-7 (2012).

Ohde T., Siegel H., *Impacts of Saharan Dust and Clouds on Photosynthetically Available Radiation in the Area off Northwest Africa*, Tellus B, **64**, (2012), doi:10.3402/tellusb.v64i0.17160.

Papayannis A., Nicolae D., Kokkalis P., Binietoglou I., Talianu C., Belegante L., Tsaknakis G., Cazacu M.M., Vetres I., Ilic L., *Optical, Size and Mass Properties of Mixed Type Aerosols in Greece and Romania as Observed by Synergy of Lidar and Sunphotometers in Combination with Model Simulations: A Case Study*, Sci. Total Environ., **500-501**, 277-294 (2014), doi:10.1016/j.scitotenv.2014.08.101.

Pappalardo G., Wandinger U., Mona L., Hiebsch A., Mattis I., Amodeo A., Ansmann A., Seifert P., Linné H., Apituley A., Alados Arboledas L., Balis D., Chaikovsky A., D'Amico G., De Tomasi F., Freudenthaler V., Giannakaki E., Giunta A., Grigorov I., Iarlori M., Madonna F., Mamouri R.-E., Nasti L., Papayannis A., Pietruczuk A., Pujadas M., Rizi V., Rocadenbosch F., Russo F., Schnell F., Spinelli N., Wang X., Wiegner M., *EARLINET Correlative Measurements for CALIPSO: First Intercomparison Results*, J. Geophys. Res., **115**, D00H19 (2010), doi:10.1029/2009JD012147.

Pérez C., Nickovic S., Pejanovic G., Baldasano J.M., Özsoy E., *Interactive Dust-Radiation Modeling: A Step to Improve Weather Forecasts*, J. Geophys. Res., **111**, *D16*, D16206 (2006), doi:10.1029/2005JD006717.

Seinfeld J.H., Pandis S.N., *Atmospheric Chemistry and Physics: From Air Pollution to Climate Change*, 2nd Edition , John Wiley & Sons, Inc, New Jersey (2006).

Shon Z.-H., Madronich S., Song S.-K., Flocke F.M., Knapp D.J., Anderson R.S., Shetter R.E., Cantrell C.A., Hall S.R., Tie X., *Characteristics of the NO-NO_2-O_3 System in Different Chemical Regimes During the MIRAGE-Mex Field Campaign*, Atmos. Chem. Phys., **8**, *23*, 7153-7164 (2008), doi:10.5194/acp-8-7153-2008.

Stefan S., Nicolae D., Caian M., *Secretele aerosolului atmosferic în lumina laserilor*, Ed. Ars Docendi (2008).

Talianu C., *Metode computaţionale pentru optimizarea, procesarea şi validarea semnalelor LIDAR*, PhD Thesis, Universitatea Politehnică, Bucureşti (2008).

Timofte A., Cazacu M.M., Radulescu R., Belegante L., Dimitriu D.G., Gurlui S., *Romanian Lidar Investigation of the Eyjafjallajokull Volcanic Ash*, Environ. Eng. Manag. J., **10**, *1*, 91-97 (2011).

Tudose G.O., Cazacu M.M., Timofte A., Nicolae D., Gurlui S., Balin I., *May 29, 2013 - a Saharan Dust Event Over Iaşi Region, Romania. Remote Sensing Observations and Regional Dust Modeling*, in: Conference on Advances in Environmental Sciences, 6th International Workshop on Optoelectronic Techniques for Environmental Monitoring, 11 - 12 June, Timişoara, Romania, 74-76 (2013).

Tudose O.-G., *Contributions to the Study of Atmospheric Aerosols Optical Properties Using Remote Sensing Techniques*, PhD Thesis, Alexandru Ioan Cuza University of Iaşi, Romania (2013).

Tudose O.-G., Cazacu M.-M., Timofte A., Balin I., *ESYROLIDAR System Developments for Troposphere Monitoring of Aerosols and Clouds Properties*, Proc. SPIE **8177**, 817716-817716–10 (2011), doi:10.1117/12.910640.

Tudose O., Tudose A., Dorohoi D., *Optics of Lidar System Used for Spectroscopic Monitoring of Air Pollution*, REV. CHIM., **66**, *3*, 426-430 (2015).

Unga F., Cazacu M.M., Timofte A., Bostan D., Mortier A., Dimitriu D.G., Gurlui S., Goloub P., *Study of Tropospheric Aerosol Types Over Iaşi, Romania, During Summer of 2012*, Environ. Eng. Manag. J., **12**, *2*, 297-303 (2013).

Welton E.J., Campbell J.R., Spinhirne J.D., Scott III V.S., *Global Monitoring of Clouds and Aerosols Using a Network of Micropulse Lidar Systems*, in: Singh U.N., Itabe T., Sugimoto N. (Eds.), Second International Asia-Pacific Symposium on Remote Sensing of the Atmosphere, Environment, and Space. International Society for Optics and Photonics, 151-158 (2001), doi:10.1117/12.417040.

Winker D.M., Vaughan M.A., Omar A., Hu Y., Powell K.A., Liu Z., Hunt W.H., Young S.A., *Overview of the CALIPSO Mission and CALIOP Data Processing Algorithms*, J. Atmos. Ocean. Technol., **26**, *11*, 2310-2323 (2009), doi:10.1175/2009JTECHA1281.1.

*** IPCC, *Climate Change 2013: The Physical Science Basis*, in: Intergovernmental Panel on Climate Change (2013).

*** RADO - Romanian Atmospheric 3D Research Observatory [WWW Document], (2015), URL http://environment.inoe.ro/category/66/rado (accessed 5.25.15).

TEHNICI MODERNE DE TELEDETECȚIE PENTRU MONITORIZAREA AEROSOLILOR TROPOSFERICI. STUDIU DE CAZ

(Rezumat)

În funcție de modul cum parametrii meteorologici variază în timp și spațiu, măsurătorile într-un singur punct oferă informații doar pentru un anumit areal specific. Astfel, o rețea de sisteme de monitorizare este benefică atât pentru prognozele meteorologice, cât și petru determinarea exactă a parametrilor de intrare în modelele de dispersie a poluanților și de studiu al atmosferei terestre pentru o zonă extinsă, astfel încât datele colectate să poată fi utilizate pentru o analiză statistică și pentru optimizarea și validarea modelelor. În acest context, începând cu anul 2010, a fost inițiată o nouă rețea de sisteme lidar la nivel național în cadrul proiectului de cercetare ROmanian LIdar NETwork (ROLINET). Un an mai târziu, a fost înființat Observatorul de

cercetare atmosferică 3D din România - RADO. Prin corelarea datelor de laborator cu măsurătorile efectuate în cadrul mai multor campanii de măsurare (măsurători efectuate de la nivelul solului până la 15-20 km altitudine), tehnicile moderne de teledetecție utilizate la nivel național și rezultate recente vor fi prezentate în această lucrare.

BULETINUL INSTITUTULUI POLITEHNIC DIN IAŞI
Publicat de
Universitatea Tehnică „Gheorghe Asachi” din Iaşi
Volumul 63 (67), Numărul 2, 2017
Secţia
MATEMATICĂ. MECANICĂ TEORETICĂ. FIZICĂ

HYDROGEN PASSIVATION EFFECT ON ZnO POWDER

BY

ELENA-VASILICA GAFTON[1,2,*], FRANCIA HAQUE[2], FRANCISCA HUŞANU[1], MARIUS MIHAI CAZACU[3,1], GEORGIANA BULAI[4] and SILVIU GURLUI[1]

[1]“Alexandru Ioan Cuza” University of Iași,
Faculty of Physics, Atmosphere Optics, Spectroscopy and Lasers Laboratory
[2]Institut des NanoSciences de Paris
[3]“Gheorghe Asachi” Technical University of Iași,
Department of Physics
[4]“Alexandru Ioan Cuza” University of Iași,
Integrated Centre for Environmental Science Studies in the
North-East Development Region - CERNESIM

Received: September 1, 2017
Accepted for publication: October 4, 2017

Abstract. The results of an experimental project concerning the optical properties of zinc oxide (ZnO) nanostructures are reported. The aim of the study is to find the origin of the yellow and the green emission bands of *n*-type ZnO sample by hydrogenation. A discussion about absorption spectra in UV-visible region was done by comparison with previous results. Parameters obtained from photoluminescence and UV absorption measurements of the ZnO powder in different stages of sample processing (in vacuum, hydrogenated before and after an annealing treatment) are discussed.

Keywords: *n*-type zinc oxide; wurtzite; photoluminescence; UV-VIS; powder hydrogenation.

[*]Corresponding author; *e-mail*: gafton.vasilica@gmail.com

1. Introduction

Zinc oxide is a chemical compound found in nature as a mineral called zincite. Synthetic ZnO is obtained as a white powder. The synthesized crystalline ZnO has a hexagonal structure, also called wurtzite. ZnO is a promising semiconductor in materials science due to its wide band gap (3.24 eV at room temperature) which makes it a good material for photonic applications in the UV-visible spectral range (Djuristic and Leung, 2006; Pankove, 1971), or its piezoelectric property which makes it adapted for electromechanical sensor (Ramadan *et al*., 2014). In addition, the high exciton-binding energy (60 meV) allows an efficient excitonic emission even at room temperature. The biocompatibility of ZnO makes him suitable in biomedical applications or in daily life products, such as cosmetics, food or sunscreen and UV absorbers (Kim *et al*., 2011). ZnO presents an advantage compared to other metal oxides that can be used for sunscreen. TiO_2 particles have to be coated with silica or alumina to avoid the formation of carcinogenic radicals which can damage the skin (Jacobs, 2010).

A variety of ZnO nanostructured morphologies have been reported (*e.g.*: such as tetrapods, nanorods, nanowires, nanorings, nanobelts). The different shapes of particles are due to various fabrication methods (Roy *et al*., 2003). Indeed, while a hydrothermal method without any metal catalyst enables the synthesis of aligned nanorods, a combustion leads to tetrapods (Zhao *et al*., 2011).

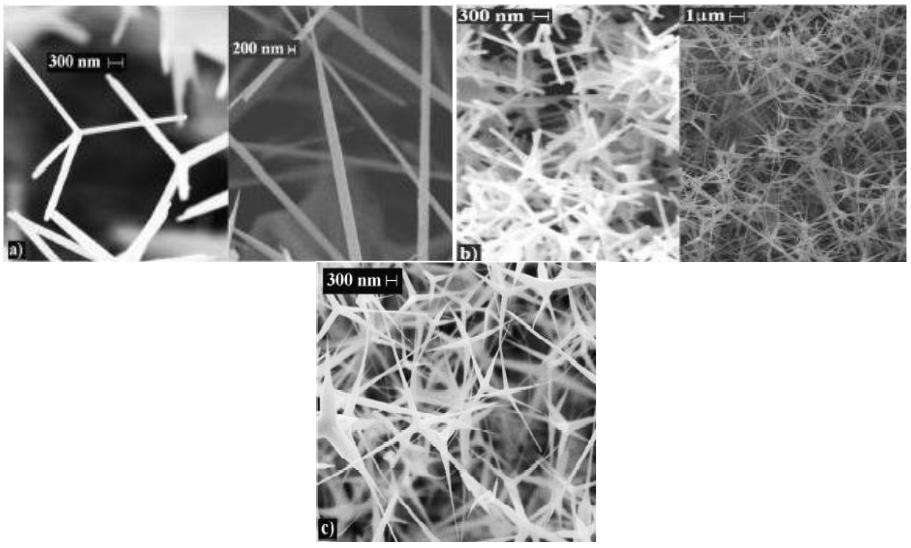

Fig. 1 – SEM images from ZnO nanostructures (Roy *et al*., 2003): (*a*) tetrapods (left) and rods (right) obtained in the air; (*b*) small tetrapods (left) and mixture of tetrapods and wires right obtained in dry argon flow; (*c*) mixture of tetrapods and wires obtained in humid argon flow.

The influence of factors such as the synthesis medium, temperature, vapor-phase or solution-phase deposition on ZnO morphology has been widely studied, but there are still several unanswered questions concerning the relationship between fabrication conditions and optical properties. Fig. 1 shows Scanning Electron Microscopy (SEM) images found in previous articles while Fig. 2 presents Tunneling Electron Microscopy (TEM) image of tetrapodal shape of ZnO particles, as reported by Roy *et al.*

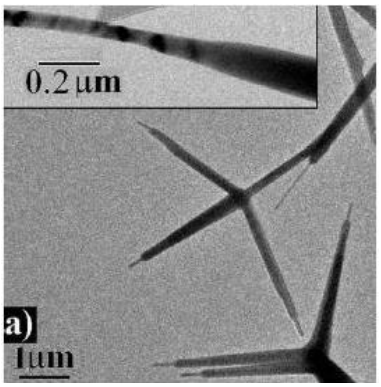

Fig. 2 – TEM images of nanowires (Roy *et al*., 2003) growing out of a tetrapod leg, inset shows a magnified image of the nanowire – tetrapod leg.

Considering that the surfaces of oxide powder particles contains a large number of defects such as steps, edges, and vacancies, which are not present on the perfect single crystal surfaces, it was interesting to study the effect of exposure to H_2 molecules at room temperature. According to literature, it is expected that the hydrogenation of the ZnO powder leads to the presence into the bulk of H atoms located at interstitial sites (Scarano *et al*., 2006; Noei *et al*., 2010; Kim *et al*., 2011).

In the present study, we focus on the hydrogenation effect on the optical properties of a sample of ZnO powder, consisting of tetrapodal particles.

2. Experimental Details

ZnO powder was synthesized by combustion method in air atmosphere. This method offers a higher purity of the final product in comparison with other synthesis techniques. The ZnO powder was prepared from the evaporation of metallic zinc pieces attached to a wire of nickel-chrome. The wire was placed in a closed chamber full of air, at room temperature and atmospheric pressure, connected to a generator. Once the wire was put in touch to the two electrodes, the zinc was brought to evaporation state by passing current through the wire; thus, the product was collected on a glass plate placed just above the zinc

sample. The ZnO product obtained as gas phase is then condensed as a white powder and transferred into a tube that will allow the removal of the moisture by pumping it into vacuum, until the pressure inside the tube reaches 10^{-4} mbar.

The sample was annealed for 1h under a dynamic vacuum of 10^{-4} mbar (Noack and Eychmuller, 2002) and activated by outgassing at 580°C, in order to remove all the impurities such as CO, CO_2 or HO^- groups which could have been adsorbed during the synthesis. In order to compensate for the oxygen loss during annealing treatment, at the end of the activation period, 120 mbar of oxygen was dosed to the sample (still kept at 580°C). After 30 min the sample was cooled and the oxygen removed by outgassing at room temperature to a final pressure of 10^{-5} mbar. The sample obtained consists of a clean *n*-type ZnO, a white powder which most probably has defects in its wurtzite crystal structure.

After the annealing process, 40 mbar of H_2 molecules were added into the tube, at room temperature. The hydrogenation of zinc oxide has been currently studied by transmission in infrared range, whose results demonstrated that exposure of mixed-terminated ZnO to atomic hydrogen leads to the metallization of the surface, whereas the exposure of the oxygen-terminated O- ZnO surface leads to the occupation of bulk interstitial sites. It was found that after exposure to H_2 molecules, there is a reversible dissociative adsorption of H_2 on both surface O and Zn sites. The H atoms are then diffusing into the bulk, and occupy interstitial sites (Noei *et al.*, 2010).

Two types of measurements were done on the obtained samples: UV-visible absorption and photoluminescence. These two complementary techniques were chosen for investigation because UV absorption gives information about the electronic transition from the ground state to an excited state, while the photoluminescence focuses on the electronic transition from an excited state to the ground state. In our case, UV absorption measurement was first done in order to have an overlook on the band gap energy of the semiconductor which was necessary in order to choose the proper excitation energy in photoluminescence measurements.

UV absorption measurements were done on a Varian Cary spectrometer. The background was measured with a pellet of barium sulphate ($BaSO_4$) by recording the reflectance intensity versus the wavelength in UV-visible range, 200-800 nm. On the surface of finally powdered sample the incident beam was diffusely scattered. The diffusely scattered beam is concentrated in the reflectance sphere. The results of reflectance were converted into absorbance using the Kubelka-Munk equation (Kubelka and Munk, 1931), Eq. (1):

$$\frac{K}{S} = \frac{[1 - 0.01\,R]^2}{2.[0.01\,R]} \tag{1}$$

where: K is the absorption coefficient, S the scattering coefficient, and R the reflectance. The energy gap was then evaluated from the UV spectra.

Photoluminescence (PL) measurements explored the effects of hydrogenation on the annealed *n*-type ZnO bulk sample. The PL spectra were obtained using a series of monochromators and a CCD camera connected to the computer. The excitation source was the 360 nm line of a Xenon laser, with a power of 450 W. The value of the excitation energy was chosen to be higher than the energy gap observed in the UV absorption measurement, in order to be able to excite electrons from the valence band to the conduction band. As a result of these transitions, the corresponding excitonic peak at 378 nm (3.28 eV) will be observed in PL spectra. A 375 nm filter was used in order to get only the photoluminescence signal. All measurements were carried at room temperature in a dark room since the photoluminescence technique is sensitive to light.

3. Results and Discussion

From the spectra shown in Fig. 3 the energy gap of the semiconductor was extracted. For the higher wavelength (low energy), the absorbance is minimum since the incident energy was not sufficient to excite the electrons. By decreasing the wavelength, the energy is enough to make electrons cross the gap, escaping from the valence band into the conduction band. So the maximum value observed for lower wavelength corresponds to the electrons absorbed in conduction band.

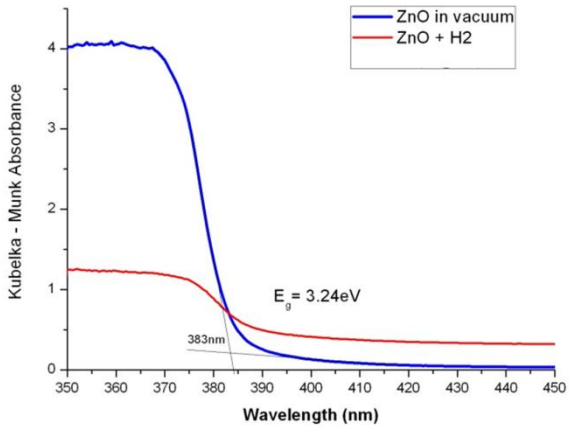

Fig. 3 – UV spectra for the ZnO particles in vacuum and hydrogenated samples.

Charge carriers are donated to the conduction band, thus providing strong evidence that H atoms diffuse into the bulk and occupy interstitial sites in a manner similar to that observed after exposure to atomic hydrogen. Absorption probes the conduction band tail of states in a *n*-type semiconductor. The tail of the valence band has been omitted since, being empty, it does not participate in the absorption process.

The results of the PL measurements of ZnO sample after synthesis, and after hydrogenation, in vacuum with a pressure of 10^{-4} mbar, at room temperature are shown in Fig. 4. For each measurement, two dominant emission peaks are observed: a near band edge ultraviolet emission peak centred around 380 nm arising from the existence of excitons, accompanied by a broad deep-level luminescence, centred on 440 nm (green) and 530 nm (yellow), and related to presence of defects as impurities or oxygen vacancies.

Both spectra were measured in the same conditions, so a comparison between the intensities may be done and the effect of hydrogenation on the sample can be observed and interpreted. It is obvious that the only effect of the hydrogenation on the as-grown sample without thermal treatment is increasing four times the intensities of the peaks due to interaction of the hydrogen with the powder.

In literature, the remarkable increase in the intensity of the bound exciton peak after hydrogenation is explained as follows: when a hydrogen atom enters ZnO, it either interacts with an impurity, such as an H donor or a carrier bound of a complex in the ZnO crystal, or it passivates a non radiative recombination centred at deep level (Khan *et al*., 2006).

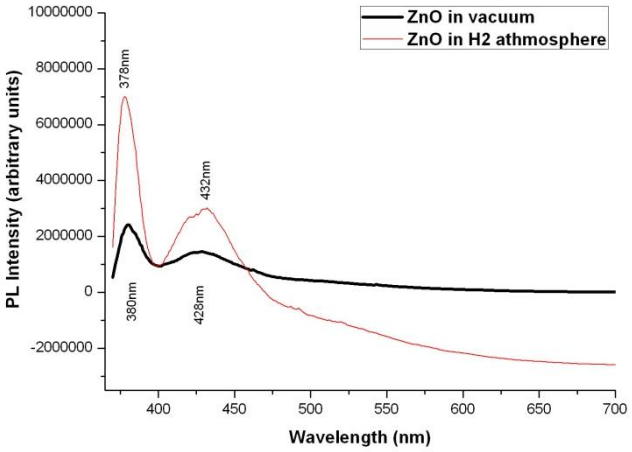

Fig. 4 – Photoluminescence spectra at room temperature of the as-grown and the hydrogenated ZnO bulk samples.

However, these results are not in totally accordance with previous ones. Kim *et al.* (2011) observed that the peak position corresponding to the defect-related wide-band emissions changes remarkably (Fig. 5). The yellow band emission peak around 2.1 eV was not present for hydrogenated ZnO, and the intensity of the green band emission peak at 2.43 eV was almost unchanged. It was concluded that the emission is related to vacancies, such as oxygen, since the yellow band is strongly passivated by hydrogen atoms after hydrogenation.

These results indicated that the yellow band emission (peak at 2.1 eV) is due to oxygen vacancies and disappears with the addition of hydrogen atoms. At the same time, it was concluded that the 2.43 eV emission peak is not related to oxygen vacancies because it remained after passivation by hydrogen atoms. Therefore, the wide defect emission was reported as due to complex vacancies and impurities or native defects.

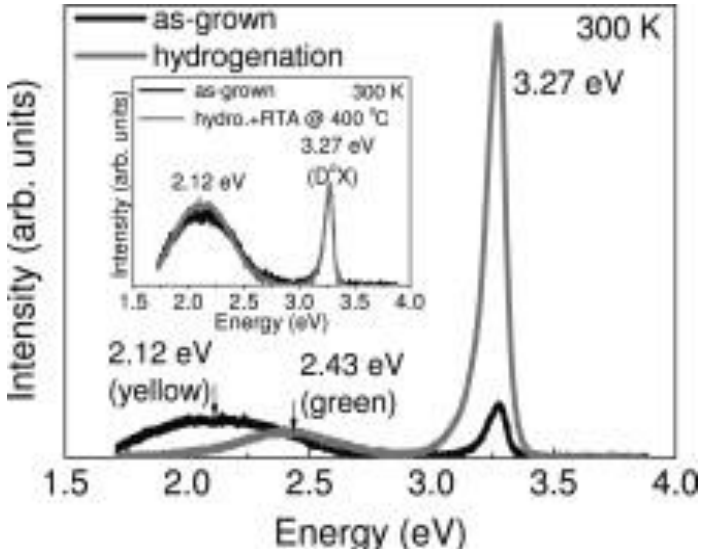

Fig. 5 – Photoluminescence spectra at room temperature of the as-grown and the hydrogenated *n*-ZnO bulk samples reported in (Kim *et al*., 2011). The inset shows the PL spectra for annealing at 400ºC of the hydrogenated sample.

The same remark as reported by Kim *et al.* (2011) can be observed in present measurements when the annealed and hydrogenated sample is taken into discussion. In Fig. 6 the PL spectra of the annealed sample at 580ºC in O_2 atmosphere, in presence of and after the H_2 outgassing is reported. An immediate observation is the increase of the peak intensities corresponding to the hydrogenated sample compared to the as-synthesized one, which is due to the interaction of the hydrogen atoms with the crystal defects.

The PL spectra of the annealed sample presents a wider peak centred at ~ 559 nm compared to the one found in Fig. 4 for the as-grown sample. This broadening is related to the emission due to transition of deep donors (as O vacancies and unknown acceptors). The peak width is due to the effect of annealing processed that created a large number of oxygen vacancies, despite the following addition of O_2 that supposed to compensate the loss of oxygen from the bulk. The intensity of the wide band emission is stronger than that of the emission peak at 380 nm.

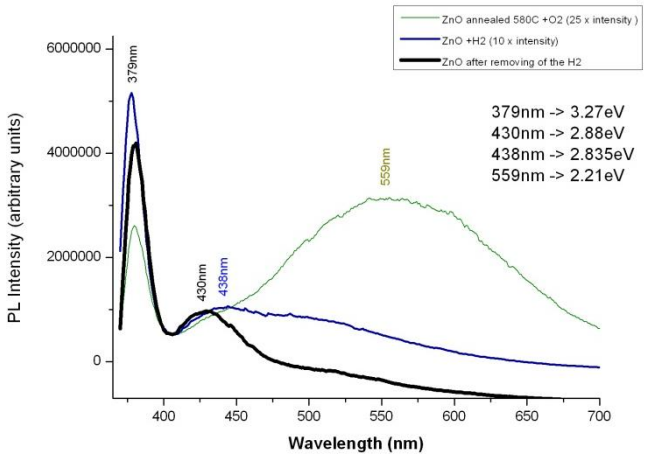

Fig. 6 – Photoluminescence spectra for annealing at 580ºC and activated in O_2 sample, in presence of and after outgassing the H_2 samples.

The intensity of the emission peak of the hydrogenated sample (blue curve) at 380 nm (3.26 eV) is significantly increased and is related to shallow donor impurities due to hydrogen addition. The emission peak at 438 nm (2.83 eV) originates from complexes between oxygen vacancies and other crystal defects. The emission peak around 550 nm is no longer present. The yellow band is strongly passivated by hydrogen atoms after hydrogenation as indicated by the enhanced optical absorption and the presence surface defect states of zinc interstitials.

The hydrogen desorption from the ZnO powder causes a 10 times decrease of the emission intensity that is clearly related to the removal of the hydrogen atoms from both interstitial and surface sites. However, the hydrogen atoms are not completely removed since the yellow band emission does not reappear (Scarano *et al*., 2006). Thus, outgassing the hydrogenated powder is not enough to remove the impurities.

The reported results indicate that i) the oxygen vacancies in ZnO are easily passivated by hydrogen atoms, ii) ionized hydrogen atoms act as shallow donors and neutralize defects and iii) a high temperature is required for hydrogen dissociation in *n*-type ZnO.

4. Conclusions

Photoluminescence measurements on synthesized, annealed and hydrogenated n-type ZnO samples were done in order to investigate the origins of the yellow and the green emission bands and the excitonic peak. After annealing, more oxygen vacancies are created, in spite of the oxygen addition,

indicated by the increase of the yellow band emission in the PL spectra. After hydrogenation, the yellow band emission does not appear anymore, due to the passivation of hydrogen atoms on the ZnO powders. This result indicates that the yellow band emission is related to the oxygen vacancies. On the other hand, the green band peak is unchanged after hydrogen passivation and is assumed to originate from complexes between oxygen or zinc vacancies and other crystal defects. Finally, the sharp peak at 3.37 eV which is the signal of the exciton is related to the shallow donor impurities due to hydrogen donors, since its intensity increases significantly after the addition of hydrogen.

Acknowledgements. This work was financial supported by the Romanian Space Agency (ROSA) within Space Technology and Advanced Research (STAR program) project number 169/20.07.2017. Authors would like to thank Slavica Stankic from Institute of NanoSciences from Paris (INSP) for fruitful discussions and Willy Daney de Marcillac from INSP for supervision during PL measurements.

REFERENCES

Djurisic A.B., Leung Y.H., *Optical Properties of ZnO Nanostructures*, Rewiews, **8-9**, 944-961 (2006).

Jacobs J.F., Ibo van de Poel, Osseweijer P., *Sunscreens with Titanium Dioxide (TiO_2) Nano-Particles: A Societal Experiment*, Nanoethics, **4**, *2*, 103-113 (2010).

Kahn M.L., Cardinal T., Bousquet B., Monge M., *Optical Properties of Zinc Oxide Nanoparticles and Nanorods Synthesized Using an Organometallic Method*, Chem. Phys. Chem., **7**, 2392-2397 (2006).

Kim M.D., Oh J.E., Kim S.G., *Hydrogen Passivation Effect on the Yellow–Green Emission Band and Bound Exciton in n – ZnO*, Solid State Comunications, **151**, 768-770 (2011).

Kubelka P., Munk F., *Ein Beitrag Zur Optik Der Farbanstriche*, Zeitschriftfür Technische Physik, **12**, 593-601 (1931).

Noack V., Eychmuller A., *Annealing of Nanometer-Sized Zinc Oxide Particles*, Chem. Matter., **14**, 1411-1417 (2002).

Noei H., Qiu H., Wang Y., *Hydrogen Loading of Oxide Powder Particles: A Transmission IR Study for the Case of Zinc Oxide*, Chem. Phys. Chem., **11**, 3604-3607 (2010).

Pankove J.I., *Optical Processes in Semiconductors*, Prentice Hall, 1971.

Ramadan K.S., Sameoto D., Evoy S., *A Review of Piezoelectric Polymers as Functional Materials for Electromechanical Transducers*, Smart Materials and Structures, **23**, *3*, 033001 (2014).

Roy V.A.L., Djurisic A.B., Chan W.K., Gao J., *Luminescent and Structural Properties of ZnO Nanorods Prepared under Different Conditions*, Applied Physics Letters, 83, 141-143 (2003).

Scarano D., Bertarione S., Cesano F., *Plate-Like Zinc Oxide Microcrystals: Synthesis and Characterization of a Material Active Toward Hydrogen Adsorption*, Catalysis Today, **116**, 433-438 (2006).

Zhao J., Han Z., Lu H., Wang X., Chen J., *Synthesis and Photoluminescence Properties of ZnO Powder by Solution Combustion Method*, J. Mater. Sci.: Mater Electron, **22**, *9*, 1361-1365 (2011).

EFECTUL DE PASIVARE A HIDROGENULUI ASUPRA PULBERII DE ZnO

(Rezumat)

Sunt raportate rezultatele unui proiect experimental privind proprietățile optice ale nanostructurilor de oxid de zinc (ZnO). Scopul acestui studiu este de a investiga natura benzilor de emisie galbenă şi verde ale oxidului de zinc de tip *n* cauzate de procesul de hidrogenare. Vor fi introduse pe scurt mai multe aplicații ale ZnO și diferite condiții de sinteză care conduc la diverse morfologii. O discuție despre absorbția în regiunea UV-VIS se va face prin comparație cu rezultate anterioare ale altor grupuri de cercetare. Sunt descrişi parametrii obţinuţi din măsurătorile de fotoluminiscenţă şi spectrosocopie UV-VIS ale pudrei de ZnO menţinută în vid, după hidrogenare, înainte și după procesul de calcinare.